Ion size dependence in electrochemical polymerization for organic 3D porous networks

A Thesis submitted to

Indian Institute of Science Education and Research Pune

in partial fulfillment of the requirements for the

BS-MS Dual Degree Programme

by

Thushar S M

Indian Institute of Science Education and Research Pune
Dr. Homi Bhabha Road,
Pashan, Pune 411008, INDIA.

April, 2023

Supervisor: Prof. Satish Patil

Certificate

This is to certify that this dissertation entitled "**Ion size dependence in electrochemical polymerization for organic 3D porous networks**" towards the partial fulfilment of the BS-MS dual degree programme at the Indian Institute of Science Education and Research, Pune represents study/work carried out by Thushar S M at the Indian Institute of Science under the supervision of **Prof. Satish Patil**, Professor, Solid state and structural chemistry unit, Indian Institute of Science, Bangalore during the academic year 2022-2023.

Prof. Satish Patil

Committee:

Prof. Satish Patil

Prof. V G Anand

Dedicated to
Friends and Family

Declaration

I hereby declare that the matter embodied in the report entitled "**Ion size dependence in electrochemical polymerization for organic 3D porous networks**", are the results of the work carried out by me at the Solid state and structural chemistry unit, Indian Institute of Science, under the supervision of Prof. Satish Patil and the same has not been submitted elsewhere for any other degree.

Prof. Satish Patil

Thushar S M

Acknowledgments

I would like to express my sincere gratitude to my supervisor, Prof. Satish Patil (IISc Bangalore) for his constant support, guidance and feedback. I also am deeply thankful to my thesis advisory committee member Prof. V G Anand, for all of our interactions over the past few years and his constant encouragement to expand my research interests which led me to my current thesis topic.

I would also like to thank my mentors, Dr Ram Kumar and Dr Anarghya Dinesh, this thesis would not be complete without their guidance, support and encouragement. I thank Dr Praveen Naik for the synthesis of all the materials studied during my thesis period.

I would like to thank all the members of the Organic Electronics research group at SSCU, IISc for all their help in the completion of this thesis as well as for all the fun times at lab, especially Manoj and Sanchari for their help with last minute experiments. I'd also like to express my gratitude to all members of Prof V G Anand lab for creating a very supportive lab atmosphere during my time there.

I would also like to thank all staff members of SSCU for maintenance of the department and instruments at SSCU.

Finally, I would like to thank my friends and family for their constant love and support without which the completion of this thesis would not have been possible.

Abstract

In the present thesis. we discuss the electrochemical polymerization of conjugated microporous polymers (CMP) and the effect of electrolyte on polymer morphology and properties. In linear conjugated polymers like PANI, polypyrrole etc., considerable work has been done related to their thin film electrosynthesis under varying conditions like electrode material, electrode preparation procedures, activation post synthesis, electrolyte etc and their effects on optical and electrochemical properties. However, trends observed in such mixed ionic-electronic conducting systems may not be assumed in other 3D conjugated porous networks like CMPs. CMPs have gained traction in the last decade due to their intrinsic porous nature and applications in photocatalysis, hole transport, energy storage, biosensing etc. Due to low solution processability, CMPs face a bottleneck in device fabrication. Electropolymerization is an effective method to synthesize thin films of CMPs. To the best of our knowledge, while many reports have studied the effect of variation in parameters like solution pH, electrolyte concentration, potential window onto the morphology of electropolymerized films, systematic reports on electrolyte variation, especially *during* electropolymerization of CMPs, are nearly nonexistent. Given the amorphous nature of CMPs and the active role of the supporting electrolyte during electrochemical polymerization, our goal in this thesis was to probe the effect of counterion variation *during* electropolymerization on various electrochemical properties like electrochromism, impedance etc as well as a primary feature of CMPs- porosity, and explore our material's application in energy storage. We varied the supporting electrolyte used during electropolymerization and analyzed the resultant film's electrochemical / optical properties using various techniques like UV-Vis spectroscopy, cyclic voltammetry, electrochemical impedance spectroscopy, spectro-electrochemistry, scanning electron microscopy and atomic force microscopy. We demonstrate the remarkable effect the choice of electrolyte can bring about in various properties of CMPs based on the resultant film's porosity and fabricate a simple supercapacitor. Compared to trends in linear conjugated polymers, ion size dependence observed for CMPs is nearly the inverse. The trend of counterion size dependence of porosity in CMPs suggests that the electrolyte choice must be treated as an important parameter to be optimized during device fabrication through electrochemical polymerization in non-controlled environments. Our study reveals direct influence of ion size on porosity in CMPs and hints towards possible ion geometry dependence in electropolymerization of CMPs.

Abbreviations

PEDOT : PSS Poly (3,4-ethylenedioxythiophene) Polystyrene Sulfonate

PANI Polyaniline

CMP Conjugated Microporous Polymers

ACN Acetonitrile

DCM Dichloromethane

THF Tetrahydrofuran

TPE-4Cz Tetra(carbazolylphenyl) ethylene

ITO Indium Tin Oxide

TBAClO$_4$ Tetrabutylammonium Perchlorate

TBAPF$_6$ Tetrabutylammonium Hexafluorophosphate

TBAOTf Tetrabutylammonium Trifluoromethanesulfonate

TEABF$_4$ Tetraethylammonium Tetrafluoroborate

KPF$_6$ Potassium Hexafluorophosphate

LiClO$_4$ Lithium Perchlorate

LITFSI Lithium Bis(trifluoromethanesulfonyl)imide

AgOTf Silver Trifluoromethanesulfonate

AgNO$_3$ Silver Nitrate

PL Photoluminescence

CV Cyclic Voltammetry

GPE Gel Polymer Electrolyte

WE Working Electrode

CE Counter Electrode

RE Reference Electrode

PRE Pseudo Reference Electrode

$\mathbf{E}_{ox_i}$ Potential at ith oxidation state

$\mathbf{C}_l$**.E** Colouration Efficiency

D.E Doping Efficiency

$\mathbf{t}_c$ Colouration Time

SEM Scanning Electron Microscopy

SPM Scanning Probe Microscopy

AFM Atomic Force Microscopy

$\mathbf{V}_{OCP}$ Open Circuit Potential

$\mathbf{R}_{CT}$ Charge Transfer Resistance

$\mathbf{R}_s$ Solution Resistance

$\mathbf{R}_{ionic}$ Ionic Resistance

IGS Isostatic Graphite Sheet

AC Activated Carbon

$\mathbf{C}_o$**.E** Coulombic Efficiency

ESR Equivalent Series Resistance

$\mathbf{C}_s$ Specific Capacitance

E.D Energy Density

P.D Power Density

Contents

List of Figures

List of Tables

Chapter 1

Introduction

In the past few decades, conjugated polymers have been studied extensively in regards to ion/electron transport. However, most such studies focus on model linear systems like PEDOT : PSS, PANI, polypyrroles etc[1–6]. Ionic/electronic transport is an important factor affecting the electrochemical/optical properties of conjugated polymer thin films, as due to their amorphous nature and active/ passive swelling in electrolytes, variation in parameters affecting ion/electron transport can affect the arrangement of polymer chains/networks allowing for further tunability and optimization of thin films for specific applications. For example, many popular conjugated polymers like PANI, PEDOT:PSS etc have been studied extensively under various parameter variations[7, 8] and thus optimized depending on the required application like electrochromism, energy storage, organic light-emitting diodes, sensors, actuators etc.

While the arrangement of polymer chains is affected in linear polymer chains, they are not porous in nature, unless the monomer used itself has an intrinsic porosity to it. Some examples of porous macromolecules are metal organic frameworks (MOF), covalent organic frameworks (COF), covalent aromatic frameworks (CAF) and conjugated microporous polymers (CMP)[9, 10]. In case of MOF/COFs, they are usually crystalline solids while CAFs are amorphous and consist of conjugated monomers but lack extended conjugation. CMPs are amorphous solids like CAFs with extended conjugation. Porosity is divided into 3 categories: microporous (< 2 nm), mesoporous (2-50 nm), and macroporous (> 50 nm). CMPs possess cross-linked structures making them porous in nature adding a different layer of complexity

compared to side chain engineering in linear conjugated polymers.

CMPs are a relatively young group of polymers, with its first synthesis reported in 2007[11]. In this short timespan, CMPs have gained significant attention for various applications like photocatalysis[12], batteries[13–17], light emittance[18], electrochromism[19–21], supercapacitors[22, 23], hole transport layers[24] and chemo/biosensing[25–27] and membranes[28, 29]. However, a major issue with most CMPs is their solution processability, which bottlenecks their ability to be processed for device fabrication since most thin film creating techniques like drop casting, spin coating etc., rely on making a solution of the polymer. Here, electrochemical polymerization is a useful procedure to generate thin films of CMPs directly onto a conductive substrate, removing the requirement of solution processability.

In linear conjugated polymers, their interaction with the supporting electrolyte during electrochemical studies can vary depending on swelling, side chain interactions, polymer chain rearrangements etc[30–41]. In the case of CMPs, recent reports have shown chemical modifications using salts leading to large variations in porosity of chemically synthesized CMPs by altering solubility related parameters[42]. As such, modification of porosity has been primarily studied through post-synthesis transformations. However, to the best of our knowledge, there exist no systematic reports on effect of salt variation in electrochemical polymerization of CMPs and its effect on porosity. In this report, we will primarily study the effect of salt variation during electrochemical polymerization and its effects on various properties and surface morphology and analyze ion size and geometry dependence in electropolymerization. We will also look at application of our polymer in an asymmetric supercapacitor.

Chapter 2

Materials and Methods

2.1 Materials and Reagents

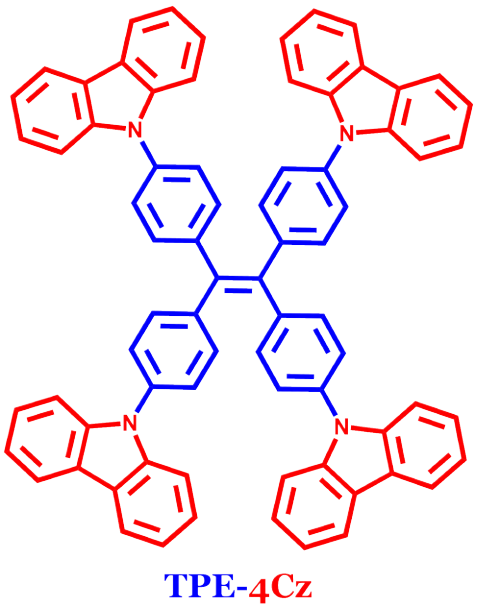

(a) TPE-4Cz

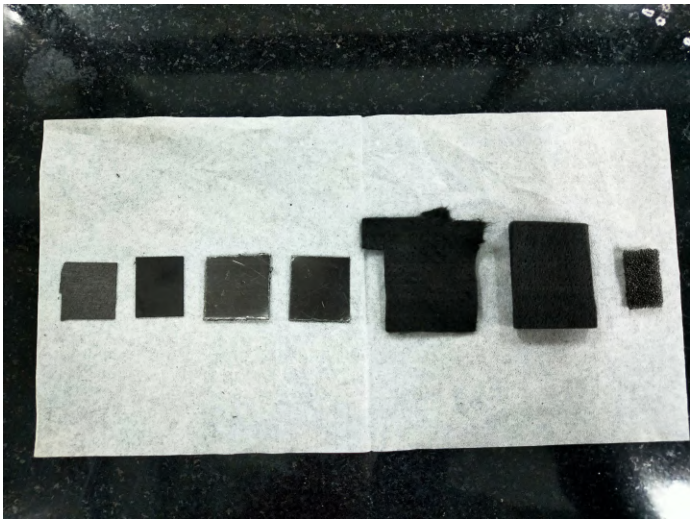

(b) from left: Toray carbon, isostatic graphite sheet, graphite plate, flexible graphite plate, 1 mm graphite felt, 6 mm graphite felt and reticulated vitreous carbon

Figure 2.1: TPE-4Cz and graphite substrates

Acetonitrile (ACN) was freshly dried before use. HPLC grade Dichloromethane (DCM), tetrahydrofuran (THF) and chloroform were purchased from Spectrochem. Supporting electrolytes - Tetrabutylammonium perchlorate ($TBAClO_4$), tetrabutylammonium hexafluorophosphate ($TBAPF_6$), tetrabutylammonium trifluoromethanesulfonate (TBAOTf), tetraethylammonium tetrafluoroborate ($TEABF_4$), potassium hexafluorophosphate (KPF_6), lithium perchlorate ($LIClO_4$), lithium bis(trifluoromethanesulfonyl)imide (LiTFSI) and standard reference silver trifluoromethanesulfonate (AgOTf) were purchased from TCI chemicals Pvt.Ltd. Sodium trufluoromethanesulfonate (NaOTf), 1-methyl 2-pyrrolidinone (NMP) and ferrocene was purchased from Spectrochem. Polymethyl methacrylate (PMMA), polyvinylidene fluoride (PVDF), lithium hexafluorophosphate ($LiPF_6$) and silver nitrate ($AgNO_3$) were acquired from Sigma-Aldrich. Indium tin oxide (ITO) [model TIX005, surface resistivity 10 Ω sq^{-1}] coated glass plates were acquired from Techinstro. Isostatic graphite sheets (IGS) and 6mm graphite felt were purchased from Nickunj eximp. 1mm graphite felt from SGL carbon, and activated carbon (AC) from SD fine chemicals Ltd. Tetra(carbazolylphenyl) ethylene (TPE-4Cz) was synthesized by Dr Praveen Naik by a literature procedure[25] (photos 2.1).

2.2 Methods and Characterization

2.2.1 Optical/Electrochemical characterization of TPE-4Cz

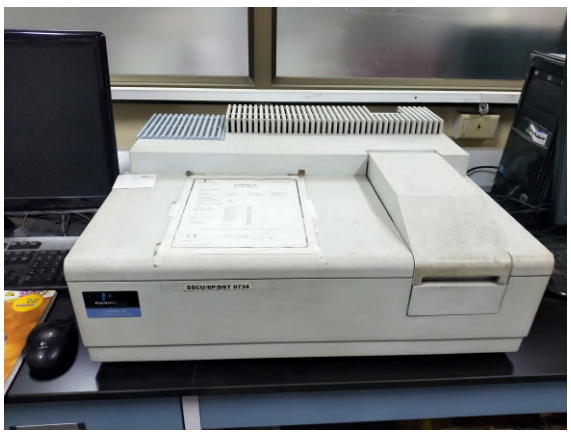

(a) Perkin-Elmer Lamda 35 instrument

(b) Fluorolog

Figure 2.2: Optical characterization instruments

UV-Vis absorption spectrum of TPE-4Cz was recorded in chloroform (10 μM) in a Perkin-Elmer (Lambda 35) UV-Vis spectrophotometer. Photoluminescence spectrum was obtained on a Horiba Jobin Yvon Fluorolog-4 spectrofluorometer (photos 2.2a).

Cyclic Voltammograms were recorded at 1 mM concentration in DCM with $TBAPF_6$ as supporting electrolyte using a CH Instruments (CHI 400A) potentiostat in a three electrode configuration with a platinum (Pt) wire as working electrode (WE), Pt coil as counter electrode (CE) and a silver (Ag) wire as reference electrode. The CV was calibrated against 10 mM ferrocene in ACN with $TBAPF_6$ as supporting electrolyte. Calibration protocol is elaborated in section 2.2.2. Highest occupied molecular orbital (HOMO) level of TPE-4Cz was computed using the onset potential (calculated by drawing a tangent at the onset of oxidation peak in the CV and noting the x-intercept) in eq 2.1:

$$HOMO = -\ [4.8 + \ (E_{onset} - \ E_{\frac{1}{2}Ferrocene})] \tag{2.1}$$

2.2.2 Electropolymerization of TPE-4Cz to PTPE-4Cz

(a) Autolab potentiostat

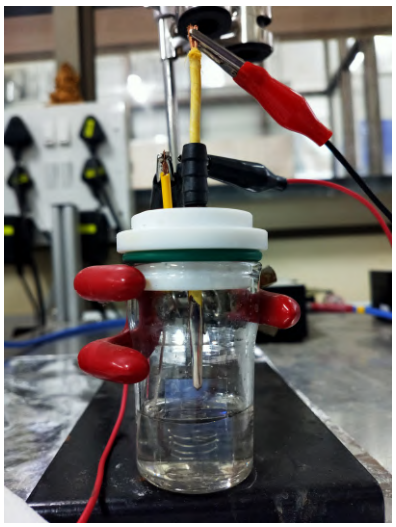

(b) custom electrochemical cell

Figure 2.3: Electropolymerization experimental setup

Electropolymerization was carried out in a custom made electrochemical cell (photo 2.3b) on a Metrohm Autolab PGSTAT302N potentiostat (photo 2.3a) with FRA analyzer using

a reported procedure[43]. Monomer solutions (0.1 mM) in a 4:1 mixture of DCM:ACN and 0.1 M supporting electrolyte in a 3 electrode configuration with a Pt coil as CE, Ag wire as RE and ITO plates/carbon based substrates (1×2.5 cm, coated area 1×1 cm) as WE. Supporting electrolytes used were $TBAClO_4$, $TBAPF_6$, $TEABF_4$, TBAOTf and LiTFSI. In the electrochemical cell, CE is always positioned opposite to the conducting side of WE and RE is positioned as close to WE as possible. This inter-electrode arrangement is maintained for all measurements. The potential window observed in the monomer CV (0 to 1.4 V) was used to potentiodynamically (repeated cycling) electropolymerize TPE-4Cz at 0.1 V s^{-1} and obtain polymer films of thickness ≈100 nm (25 cycles). All polymerization and CVs have been done at 0.1 V s^{-1} unless mentioned otherwise. Thickness profiles were measured using a Bruker Dektak XT surface profilometer.

Since Ag wire is a Pseudo reference electrode (PRE), for accurate idea of the position of redox peaks, all CVs were calibrated against Ferrocene (Fc/Fc^+, $E_{\frac{1}{2}}$= 0.080 V vs Ag/Ag^+, $E_{\frac{1}{2}}$= 0.054 V vs SHE). Ferrocene solutions were made at 10 mM concentrations with all other conditions identical to the monomer/ monomer-free solution. The reference electrode was calibrated against Ferrocene, before and after CV measurements of (P)TPE-4Cz . $E_{\frac{1}{2}}$ of Fc/Fc^+ couple were then averaged to obtain the reference zero potential for TPE-4Cz's electropolymerization and monomer-free CVs.

For UV-Vis and Fluorescence spectrum of thin films, 50 cycles at 0.2 mM monomer concentration was used. For Spectro-electrochemistry, 2×2 cm area was coated by electropolymerizing using 0.4 mM solution for 25 cycles. For device fabrication, 0.4 mM solution was used for 25 cycles.

2.2.3 Characterization of PTPE-4Cz

Post-polymerization the films were washed with THF and ACN to remove excess monomer and electrolyte. Monomer-free CVs were done in ACN with 0.1 M of the respective supporting electrolyte. HOMO level of the polymer was calculated using equation 2.1.

UV-Vis and spectro-electrochemistry was performed on an Ocean Optics instrument with a DH-2000-BAL UV-Vis-NIR lightsource, ocean FX-XR1-ES and NIR 512-2.5 visible and NIR photodetectors. Fluorescence spectra of the films were recorded on Horiba Jobin Yvon

Fluorolog-4 spectrofluorometer.

Spectro-electrochemistry experiments were done in a MM Spectro-EFC, SMA 905, 1.75 mL - magnetic mount optical fiber spectro-electrochemical flow cell from redoxme AB. The transmission spectra was recorded every 500 ms within the potential window 0-1.4 V for all supporting electrolytes (0.1 M/dry ACN) with the exception of $TEABF_4$ which required 0-1.55 V.

Transient switching kinetics were studied at ion insertion potentials monitoring a wavelength of interest. Following pulse widths were used (number of pulses in brackets) : 100 ms (150), 500 ms (75), 1 s (75), 3 s (20), 5 s (12), 10 s (6), 20 s (3) Time required to reach 95% of the total transmittance change (t_{95}) was calculated by applying a square wave pulse for 5 s of colouration and 5 s of bleaching. Other figures of merit were calculated using the following equations:

$$\Delta T\ (\%) = a(1 - e^{-bx}) \tag{2.2}$$

$$Doping\ efficiency\ (D.E) = \frac{Charge\ output}{Charge\ input} \tag{2.3}$$

$$Colouration\ efficiency\ (C_l.E) = \frac{\Delta OD}{q/A}(cm^2C^{-1}) \tag{2.4}$$

Where:

ΔT (%) : Change in Transmittance

a : Max change in Transmittance (ΔT $(\%)_{Max}$)

b : $1/\tau$, τ = time constant

x : pulse width (s)

ΔOD : Change in optical density between colourless neutral and coloured state

q/A : charge injected per unit area (here A=1.1 cm^2)

For colourimetric analysis, CIELAB (CIE 1976 standard) co-ordinates were obtained in reflectance mode (every 500 ms/ 0.05 Vs^{-1}). Colour difference (ΔE^*_{ab}) values were calculated using eq 2.5:

$$\Delta E^*_{ab} = \sqrt{(a^*_2 - a^*_1)^2 + (b^*_2 - b^*_1)^2 + (L^*_2 - L^*_1)^2} \tag{2.5}$$

where L*, a* and b* are coordinates in CIELAB (CIE 1976 standard) colour space. Points are chosen at the extremities of the potential window.

EIS measurements were done on the Metrohm Autolab in the frequency range 100 mHz - 0.1 MHz with amplitude set to 50 mV on ion insertion potential. Measurements were done on a single film for both oxidation states after performing CV. For carbon based substrates, EIS was measured at the open circuit potential (V_{OCP}) [recorded for 60 s, dE/dt limit disabled]. For devices, EIS was measured at (V_{OCP}) [recorded for 200 s, dE/dt limit disabled] in the frequency range 10 mHz - 0.1 MHz with amplitude set to 10 mV of the open circuit potential (V_{OCP}). EIS curve fitting was done using Zsimpwin software. Volumetric Capacitance (C_{vol}) for single electrodes was calculated using eq 2.6:

$$C_{vol} = \frac{1}{2\pi f Z'' V} \tag{2.6}$$

where **f** is the frequency, **Z"** is the complex part of impedance and **V** is volume of the film.

SEM imaging for thin films on carbon based substrates was done by Dr Anarghya on a SEM with MonoCL at MNCF, CeNSE, IISc. Surface metrology of the films was investigated by AFM in tapping mode over a 10 μm $\times$ 10 μm area on a Cypher ES environmental AFM by Manoj Sharma.

2.2.4 Half cell/Two electrode studies

Polymers NDI-NDI-OD-TEG, NDI-NDI-2OD and monomer DPP-Hex-CN4 were drop casted while highly conductive PEDOT:PSS was spincoated onto ITO plates. Activated carbon was coated onto IGS. NDI-NDI-OD-TEG was tested in a gel polymer electrolyte (GPE) while the rest, in a reaction vessel.

2.2.5 Device fabrication and optimization

IGS were cut into 2×2.5 cm pieces. WE was made by electropolymerizing PTPE-4Cz_TFSI onto IGS (blocking one side with thin adhesive tape). AC was coated on IGS by creating

a slurry of 85 wt% AC with 10 wt% Ketjen black and 5 wt% binder (PVDF in NMP). A 1.27×1.27 cm well was made by punching a hole into transparent double-side adhesive tape to pour GPE into and the tape acts as a separator for the electrodes.

GPE were prepared by heating 1:2 mixture of propylene carbonate (PC) (3 mL) and ACN (6 mL) with 0.45 g salt and 1.05 g PMMA at 65 °C overnight. Salts that were used to make GPE - $TBAPF_6$, NaOTf, $TEABF_4$, KPF_6, LiTFSI, and $LIClO_4$.

Concentration variation of salt in GPE was tested after the choice of supporting electrolyte was optimized, changing the ratio of salt:PMMA to 1:1. AC electrode's mass loading was varied from 0.5 to 2.5 mg/cm^2 to minimize dead weight on electrode. The actual active area of device was 1.6 cm^2. Coulombic efficiency (C_o.E), equivalent series resistance (ESR), specific capacitance (C_s), energy and power density (E.D, P.D) of the devices were calculated from GCD curves (every 10th cycle) using the following equations:

$$C_o.E\ (\%) = \frac{Discharge\ time}{Charging\ time} \tag{2.7}$$

$$ESR\ (\Omega) = \frac{\Delta V_{CD}}{Current} \tag{2.8}$$

$$C_s\ (Fg^{-1}) = \frac{2 \times I \times \Delta t}{m \times \Delta V} \tag{2.9}$$

$$Energy\ Density\ (Wh\ kg^{-1}) = \frac{C_s \times (\Delta V)^2}{2 \times 3.6} \tag{2.10}$$

$$Power\ Density\ (W\ kg^{-1}) = \frac{Energy\ Density \times 3600}{\Delta\ t} \tag{2.11}$$

Where:

ΔV_{CD} : Peak charging potential - Peak discharging potential

C_s : Specific Capacitance

Δt : Discharge time

m : Active Mass of both electrodes

ΔV : Potential window

Chapter 3

Results and Discussion

In order to study effect of counterion variation on properties like porosity in electropolymerized films of CMPs, we chose the molecule TPE-4Cz, for its ease of synthesis and prior literature in different applications[25, 43–45]. Counterion, by definition is an ion accompanying a charged species to maintain electrical neutrality. An integral part of electrochemical polymerization is the formation of radical cations leading to an electrochemical analogue of oxidative chemical polymerization. This loss of electron leads to the formation of a potential difference between the electrodes. For maintaining electrical neutrality during electrochemical oxidation, the counterion from bulk electrolyte diffuses into the polymer film to balance the charge created by the loss of electron. This process is known as electrochemical doping. During reduction, the potential difference created lets the counterions diffuse back to the bulk electrolyte. This is also known as electrochemical dedoping.

3.1 Characterization of Monomer

TPE-4Cz is a white fluffy material with a molecular weight of 993.23 g mol^{-1}. Prior to electropolymerization, it is important to understand the optical and electrochemical behaviour of the monomer. With that in mind, we recorded its UV-Vis (200-1050 nm) . Excluding the two characteristic peaks of carbazole in the range 290-310 nm, two peaks are observed at 255 nm and 294 nm (Figure 3.1b). CV of the monomer in DCM shows two distinct peaks at 0.75 and 1.05 V, which, from previous reports, are attributed to the oxidation of the TPE

core and irreversible oxidation of carbazole moeities respectively (Figure 3.1c). HOMO level of the monomer was calculated to be -5.39 eV from the CV.

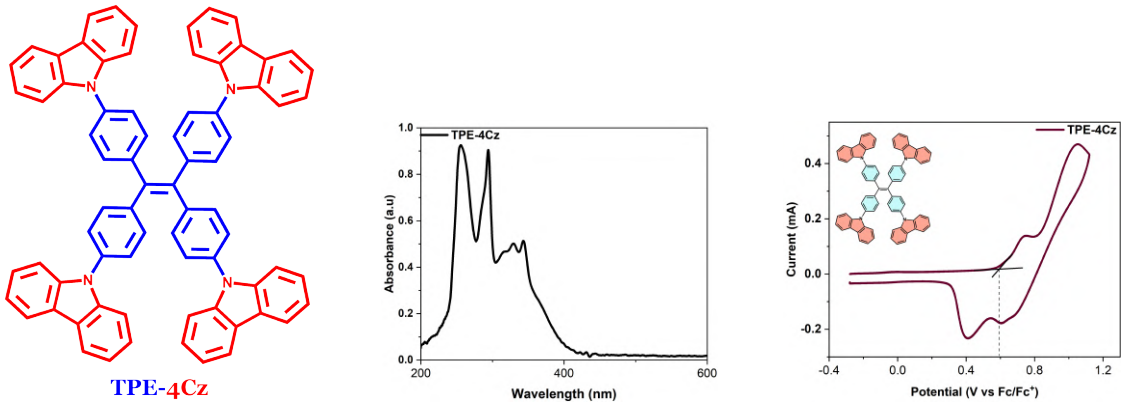

(a) Chemical structure (b) UV-Vis spectrum (c) Cyclic Voltammogram

Figure 3.1: Optical and electrochemical characterization of TPE-4Cz

3.2 Electropolymerization and characterization

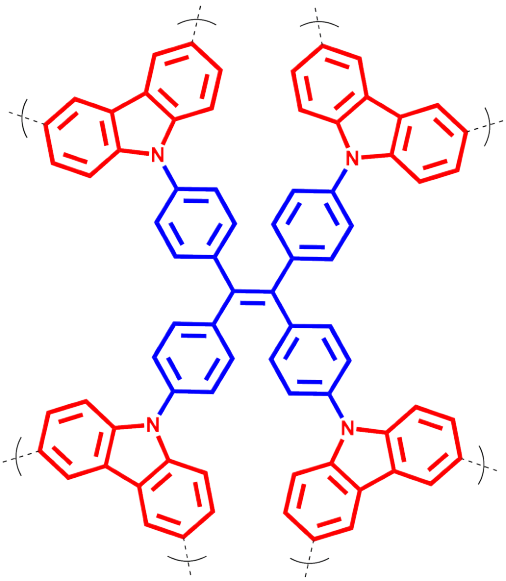

Figure 3.2: Cross linked structure of PTPE-4Cz

We attempted electropolymerization of TPE-4Cz using supporting electrolytes with anions of various sizes like ClO_4, PF_6, BF_4, OTf and TFSI. The polymerization CVs and

monomer free CVs show two reversible redox peaks at slightly different potentials dependent on the counterion (see figure 3.3a, 3.3b). Electrochemical polymerization proceeds through the formation of a radical cation species (here the aforementioned irreversible oxidation of the carbazole moiety). the radical cation then proceeds to dimerize forming a dication. The peaks we see in polymerization CV is of the oxidation of the bicarbazole group to the radical cation and dication species. From previous reports, we can conclude that the connectivity of the polymer is at the 3,6 positions of carbazole[43, 44]. With every cycle, we can notice the increase in current density at the redox peaks, signifying the growth of polymer film on the working electrode surface. Interestingly, in the case of TBAOTf, we were not able to polymerize the films beyond a thickness of 50 nm. The CV profile during electropolymerization with TBAOTf (figure 3.4) shows a very different profile compared to other counterions. Due to very low thickness of films and poor CV response, studies with OTf were discontinued. However, topography analysis was done on OTf films for further investigation into their unusual behaviour (section 3.4).

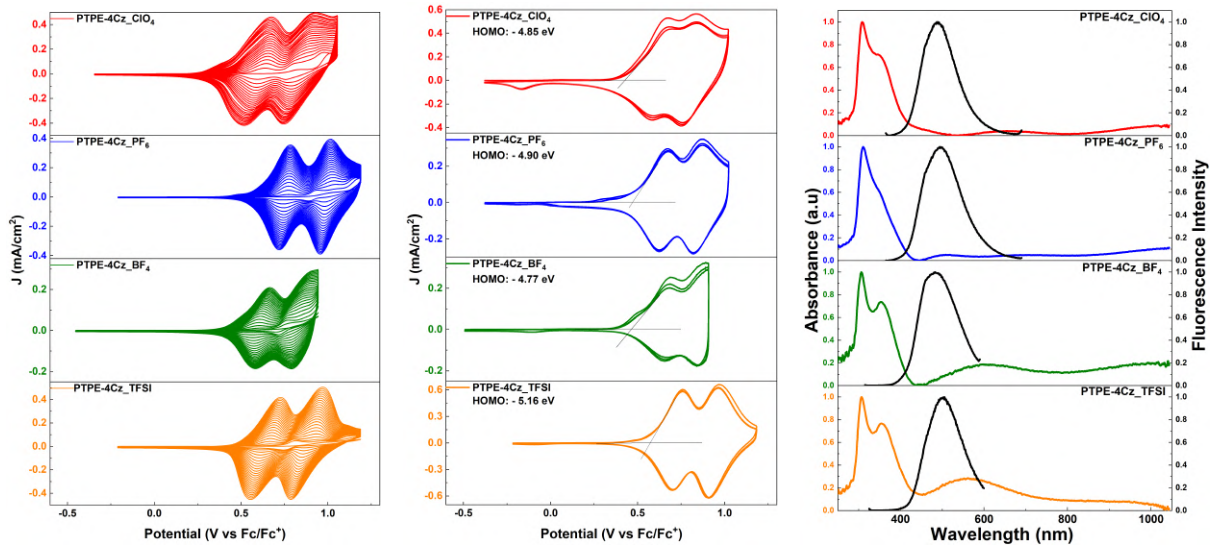

(a) CV profiles during electrochemical polymerization

(b) Monomer free CVs

(c) UV-Vis and PL spectra

Figure 3.3: Optical and electrochemical characterization of PTPE-4Cz

The polymers show electrochromism (green and blue) during polymerization and CV at the first and second oxidation peaks respectively, with the notable exception of OTf based films showing no electrochromism . Since PTPE-4Cz is a conjugated system, during oxidation to the radical cation/ dicationic state, its band gap could lie in the visible region in these

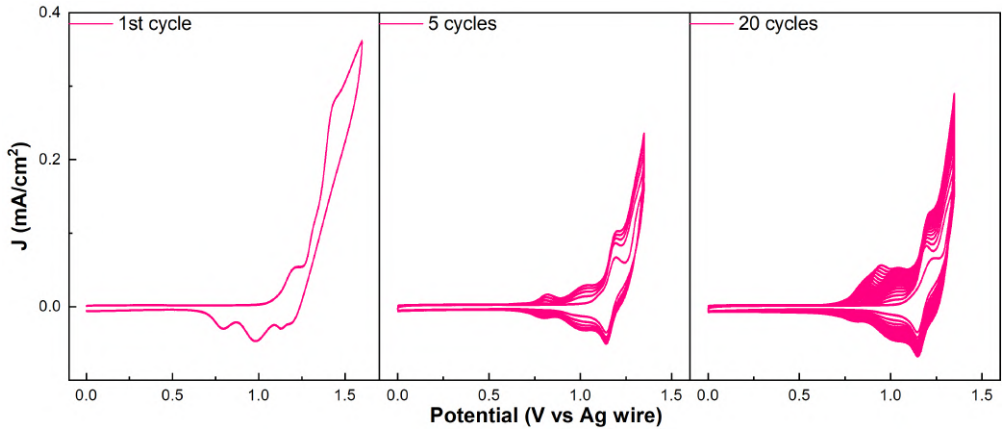

Figure 3.4: Polymerization CV profile of TPE-4Cz in TBAOTf

states giving rise to the observed electrochromic behaviour. In figure 3.3c and table 3.1, it can be seen that the effect of counterion on the optical spectra appears to be negligible, with a prominent peak in the UV region ($\approx$ 310 nm) and two broad low intensity peaks in the visible and NIR region respectively. Exciting the polymers at wavelengths close to 310 nm gives rise to a peak ($\approx$490 nm) in the PL spectrum. At the least, any (if) changes in porosity from counterion variation is not affecting the optical properties in neutral state. However, this cannot be assumed during electrochemical (de)doping.

Counterion used	E_{ox_1} (V)	E_{ox_2} (V)	UV-Vis peak	PL peak
ClO_4	0.68	0.84	297	490
PF_6	0.67	0.88	299	494
BF_4	0.68	0.90	307	483
TFSI	0.75	0.96	310	505

Table 3.1: Oxidation potentials and optical spectra peaks of PTPE-4Cz

Considering PTPE-4Cz is a conjugated polymer network, there must be (bi)polarons forming in the polymer during electrochemical (de)doping, which is essentially the counterion from electrolyte solution diffusing into the polymer film to balance the loss of electron during electrochemical oxidation (doping) and their diffusion back to solution during electrochemical reduction (dedoping). Since this process occurs in every CV cycle, the geometry and size of the counterion must play some role in the arrangement of CMP networks, for ex:

during dedoping, a larger counterion *may* leave behind larger pores in the polymer network, thus affecting porosity. This, as such, is currently only a hypothesis and requires further experiments for a clear picture. Depending on whether the counterion has an effect on the porosity, there are a few possibilities we can investigate:

- In case of negligible effect of counterion and :
  - formation of small sized pores in all films, smaller counterions must have the size advantage in diffusion.
  - formation of large size pores in all films, all counterions must show similar ion transport.
- An additional factor to account for is the strength of interaction between the polymer backbone and the counterion. Smaller ions may interact strongly due to low polarizability leading to inefficient dedoping while larger counterions are easily polarizable resulting in weaker interactions with the backbone.

These factors affecting polymer morphology could also affect electrochromic properties, since electrochromism also depends on factors like doping efficiency which would show variation in case of porosity difference between PTPE-4Cz made with different salts. While some slight differences in the intensity of electrochromic behaviour was noticed in CVs (reaction vessel), to quantify this colour change and compare between counterions, we need to obtain optical spectra *during* potential sweeps. To probe the aforementioned possibilities and build onto a theory of counterion variation's effect on CMP electrosynthesis, spectro-electrochemistry experiments were carried out in order to investigate effect of counterion on the electrochromic properties of PTPE-4Cz (elaborated in section 3.3) All figures henceforth are color coded w.r.t the counterion employed- ClO_4- Red, PF_6- Blue, BF_4- Green and TFSI- Orange.

3.3 Spectro-electrochemistry and EIS of PTPE-4Cz

Spectro-electrochemistry is a kind of *in-situ* spectroscopy where the material under study is subjected to a potential bias/sweep and the optical (or in other cases: NIR, Raman, PL,

NMR etc) spectra is simultaneously recorded. This lets us assign (bi)polaronic peaks in the recorded spectra to redox peaks in CV. Reflectance mode allows for the collection of CIELAB colour coordinates (and other CIE values). ΔE^*_{ab} values can be obtained from the CIELAB coordinates. Switching time experiments let us calculate various figures of merit like Doping efficiency, colouration efficiency, standard switching time and t_c. Such information can give us a better picture of the effect that counterion choice has during electropolymerization.

3.3.1 Counterion effect on Transmission spectra

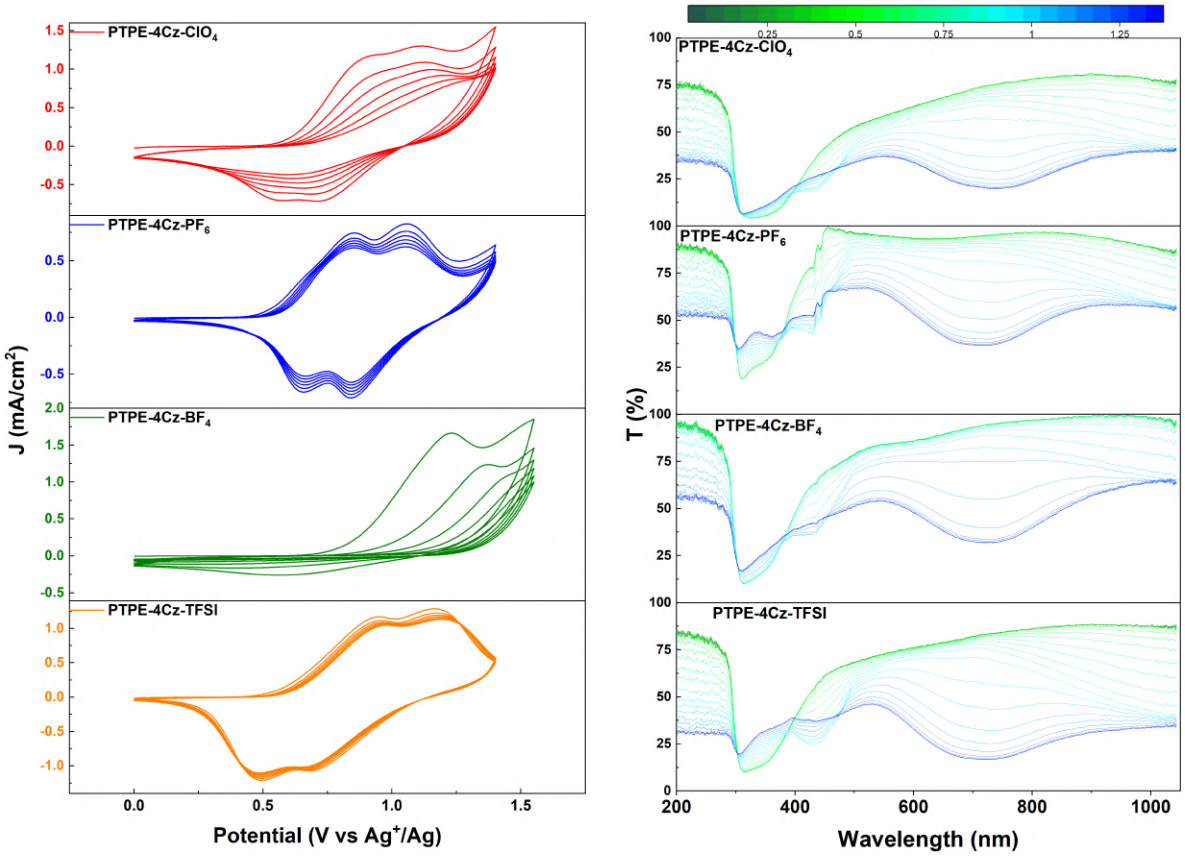

(a) CV during spectroelectrochemistry (b) Transmission spectra during CV

Figure 3.5: CV and transmission (%) spectra collected *in situ*

During Spectro-electrochemistry , we observe that films made using smaller counterions like ClO_4 and BF_4's CV degraded extremely quickly (figure 3.5a), while larger counterions (PF_6 and TFSI) were much more stable. From the CV, we can also observe that during dedoping, ClO_4 and BF_4 are not able to dedope completely from the polymer films. Since

PTPE-4Cz does not have any side chains that favour ion transport, the effect of salt-polymer backbone interactions must not be significant. If it did, we should have been able to observe this during the polymerization process itself. But this possibility still cannot be ignored.

From our previous discussion on possibilities of counterion effect during electropolymerization in section 3.2, we can conclude that the porosity in the films are *not* of the same size at the least, since :

1. Smaller counterions do not display better ion transport than their larger counterparts, but in fact perform worse. This implies that the pore sizes are at the least, not small in size. Larger counterions showing better doping also corroborates this conclusion as these ions must be able to diffuse into the films during doping, which wouldn't be possible without large enough pores.

2. In case of larger pore sizes, smaller counterions should have dedoped efficiently, or even shown higher doping efficiency since more small size ions should be able to enter larger pores. However, this is not what is observed, indicating all of our films must have some variation in porosity.

This leads to a hypothesis that in films made using smaller counterions, ions may not be able to dedope efficiently as with no sufficient pore size, rapid influx and efflux of ions at doping potentials could rapidly compromise the structural integrity of the polymer, which indicates a positive correlation between counterion size and PTPE-4Cz's porosity. In the transmission spectra (figure 3.5b), we observe that the ΔT (%) values for the (bi)polaron bands at $\approx$430 nm and $\approx$750 nm are varying w.r.t the counterion.

In order to test our hypothesis of counterion size vs porosity, we performed switching time experiments and colourimetric analysis (elaborated in section 3.3.2).

3.3.2 Transient switching kinetics

Switching kinetics experiments were studied by repetitive application of a square wave potential step corresponding to ion insertion and monitoring ΔT (%) where max change is observed. The square wave's pulse was varied from 100 ms to 10 s. Table 3.2 shows the parameters used for switching time experiments.

Counterion used	E_{ox_1}(V)	E_{ox_2}(V)	λ_{ox_1}(nm)	λ_{ox_2}(nm)
ClO_4	0.85	1.05	430	750
PF_6	0.85	1.05	430	720
BF_4	0.90	1.5	430	750
TFSI	0.95	1.25	430	730

Table 3.2: Potentials and wavelengths used to monitor switching kinetics

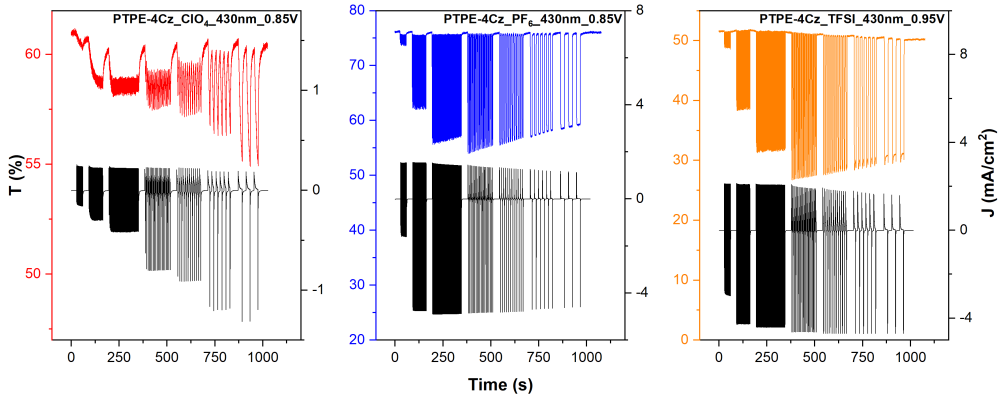

(a) Transmission spectra and chronoamperometry data corresponding to E_{ox_1}

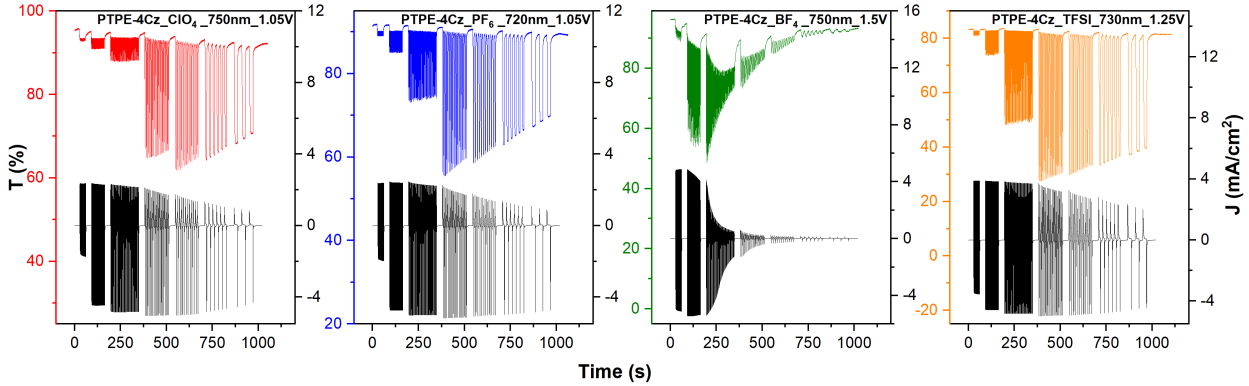

(b) Transmission spectra and chronoamperometry data corresponding to E_{ox_2}

Figure 3.6: Ion size dependent switching kinetics of PTPE-4Cz

At E_{ox_1}, In case of smaller counterions, ClO_4 shows very little ΔT (%)($\approx$5% at max) overall while BF_4 shows negligible/ undetectable levels of switching. PF_6 and TFSI on the other hand, show much better switching stability as well as 4-5x higher ΔT (%)(20-25%) (figure 3.6). If the porosity of the polymers were of a similar but small size, theoretically smaller counterions should have had a size advantage in ion transport resulting in rapid

saturation of ΔT (%) values at lower pulse widths. But here, we are noticing the exact opposite with larger counterions showing better switching kinetics as well as rapid saturation at lower pulse widths. This adds up to our results in sections 3.2 and 3.3.1, giving further evidence of porosity variation during polymerization.

At E_{ox_2}, surprisingly, all counterions show appreciable ΔT (%) values, although the BF_4 based film does degrade rapidly with increasing pulse width, hinting at an inability in stabilizing the dication state of PTPE-4Cz. Inexplicably, ClO_4 shows far better switching stability with E_{ox_2} than E_{ox_1}. PF_6 and TFSI show even higher ΔT (%) values at E_{ox_2} than E_{ox_1}, which suggests that the increase in ΔT (%) observed in ClO_4, PF_6, and TFSI at E_{ox_1} could imply the dication's stability to be higher in comparison to the radical cation.

From figure 3.6, we calculated various figures of merit summarised in table 3.3. Quantities calculated were maximum contrast [ΔT (%) = $T_{bleaching}$(%) - $T_{coloured}$(%)], doping efficiency, colouration efficiency, standard switching time (t_{95}) and colouration time (t_c) (Methods related to calculation of figures of merit elucidated in section 2.2.3). ΔT $(\%)_{Max}$ value reported was taken to be 95% of maximum ΔT (%). t_{95} was calculated from fitting ΔT (%) vs pulse width.

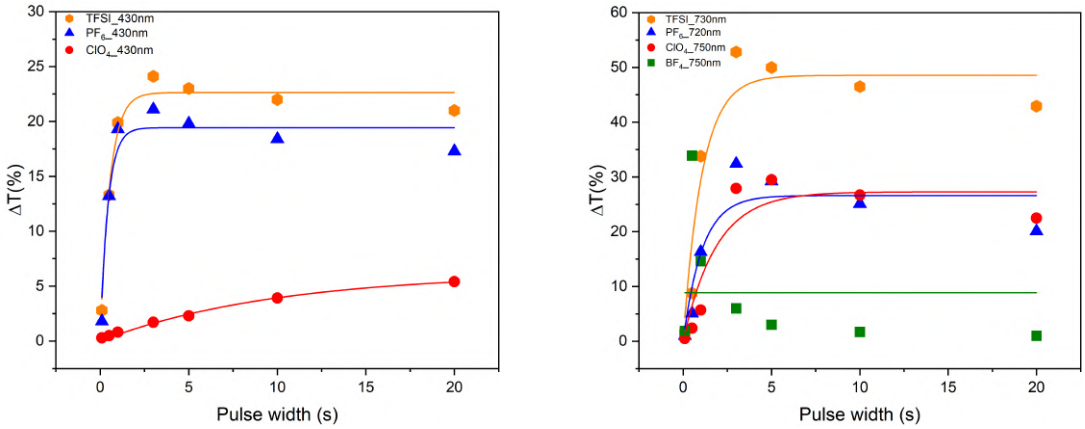

(a) at E_{ox_1} (b) at E_{ox_2}

Figure 3.7: Fitted curves of ΔT (%) vs pulse width

Fitting ΔT (%) vs pulse width (figures 3.7a, 3.7b), t_{95} calculated does not match well with t_c calculated from experimental data. In general, the fitting overestimates switching time to switch between bleached and coloured states. Coupling this with the rapid reduction in transmittance seen during switching times >1 s (figure 3.3.2) in all the polymers, this

Polymer @wave-length(nm)	**ΔT (%)$_{Max}$**	**t_{95} (s)**	**t_c (s)**	**D.E**	**C_l.E**
ClO_4_430	2.34	9.91	4.61	92.34	37.02
ClO_4_750	29.46	1.85	4.08	76.89	66.04
PF_6_430	18.66	1.30	1.83	71.79	130.41
PF_6_720	29.17	3.25	3.18	70.63	74.63
BF_4_750	3.00	-	3.90	33.80	34.47
TFSI_430	22.64	1.62	3.53	88.33	78.23
TFSI_730	49.96	3.22	2.84	81.93	81.33

Table 3.3: Table of figures of merit for PTPE-4Cz.

suggests that PTPE-4Cz's switching kinetics is more stable at pulse widths <1 s. Relating the figures of merit to our discussion on ion size dependent porosity, it is evident that larger anions (TFSI/PF_6) show much higher doping efficiency than BF_4. However, ClO_4's D.E is extremely high in E_{ox_1}, albeit the actual ΔT (%) value is very low. This high D.E as well as relatively high C_l.E of ClO_4 compared to BF_4 does not allow us to come to a conclusion on ion size dependence as this gives rise to two possibilities:

1. ClO_4's doping kinetics may be affected by low porosity, which should actually give rise to inefficient volumetric doping.
2. ClO_4's doping kinetics are reflected in its D.E and C_l.E values suggesting ClO_4's inefficient dedoping is connected to ion-polymer backbone interactions.

It must be noted that our discussion with switching kinetics experiments have primarily allowed us to link dedoping inefficiency with anion size. This does not give us much clarity on volumetric doping efficiency, however. IF poor ion transport kinetics were only observed during electrochemical dedoping, then we can conclude that the dedoping inefficiencies in smaller anions is related to their low polarizability and stronger interactions with the charged polymer network. To compare the efficiency of volumteric doping between anions, colourimetric analysis was done based on CIELAB colour coordinates at ion insertion potentials (section 3.3.3).

3.3.3 Colourimetric Analysis

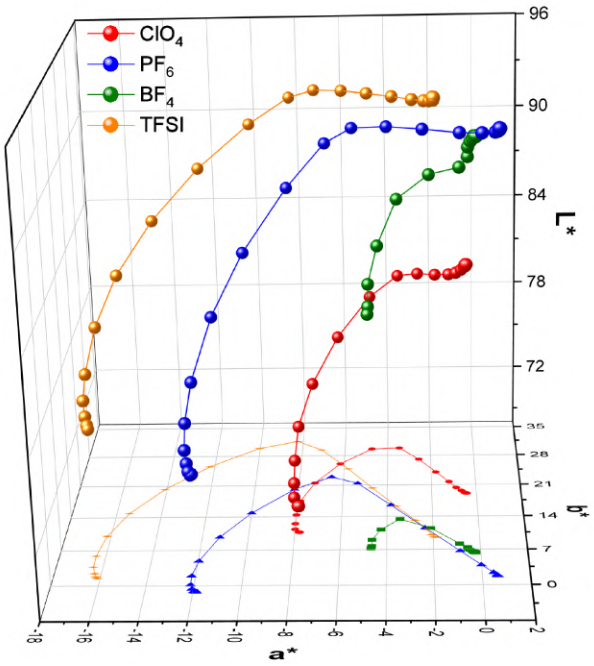

Figure 3.8: Path of $L^*a^*b^*$ coordinates during forward potential sweep relative to anion

Colourimetric analysis was carried out based on the "Commission Internationale de l'Eclairage" (CIE) 1976 L^* a^* b^* standards. L^* denotes perceptual lightness (0=black, 100= diffuse white), a^* axis represents green (-ve) and red (+ve) and b^* represents blue (-ve) and yellow (+ve).

Figure 3.8 depicts the path of $L^*a^*b^*$ coordinates in 3D colour space as the potential is sweeped from neutral to fully oxidized states for the polymers. Figure 3.9 represents the a^*b^* space/xy projection of the 3D path of the coordinates during the potential sweep from neutral to electrochemically fully doped state. The plot also shows the CIE L^* a^* b^* colour of the films upon complete oxidation. Table 3.4 contains the CIELAB coordinates at ion insertion potentials as well as the corresponding colour and ΔE^*_{ab} values. At 0.85/0.95 V, while L* values don't see a large diference, a* becomes increasingly negative with increase in anion size, indicating larger changes in the green region of the colour space. In BF_4's case, we see almost no difference in b* value, implying a much lower change in the yellow region in comparison to the other anions. Interestingly, smaller anions show very little change in colour upon reaching E_{ox_1}. the lower a* value in ClO_4 and BF_4 results in a faint khaki colour at E_{ox_1}, while a distinct fall green colour is observed in PF_6 and TFSI's case.

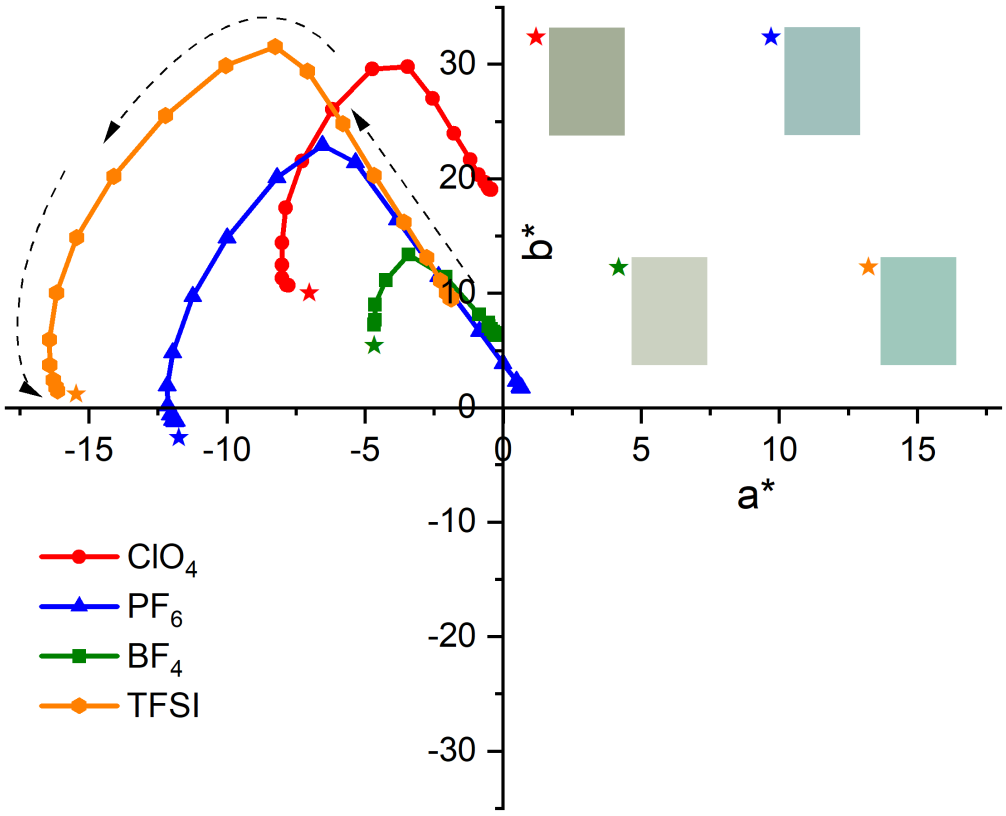

Figure 3.9: Plots of a^* b^* colour coordinates collected at 0.05 V intervals from neutral(0 V vs Ag^+/Ag) to fully oxidized states(1.4 V for ClO_4, PF_6, TFSI and 1.55 V for BF_4). Dashed arrows indicate potential sweep direction and resultant colour variation. Highlighted zones with symbols display colour of film upon complete electrochemical doping

at E_{ox_2}, large anions' b* value decrease by a large extent, indicating a shift from the yellow region and closer to the blue region in colour space, resulting in a shadow green shade. ClO_4 and BF_4 do not show much change in the b* region over this transition, showing a dark khaki and foggy grey colour respectively. The low ΔE^*_{ab} and negligible colour changes in ClO_4 and BF_4 over the potential sweep suggest that these smaller anions are unable to induce efficient volumetric doping in the bulk of the polymer film.

Adding to our discussion in section 3.3.2, we can finally conclude that the cause for worse (de)doping kinetics of smaller anions cannot be from ion-polymer interactions, but rather, is due to the lower porosity of films made with these anions. To obtain conclusive visual conformation to our hypothesis, AFM of thin films' morphology was investigated to analyze the porosity and surface roughness (section 3.4).

Anion	Potential (V)	CIE (L*, a*, b*)	Colour	ΔE^*_{ab}
ClO_4	0	(83.214, -0.481, 19.079)		17.5
	0.85	(81.444, -1.785, 23.971)		
	1.05	(76.808, -6.183, 26.038)		
PF_6	0	(95.073, 0.627, 1.761)		23.4
	0.85	(91.464, -5.35, 21.416)		
	1.05	(82.285, -11.237, 9.741)		
BF_4	0	(93.735, -0.255, 6.403)		11.7
	0.95	(97.723, -0.315, 6.509)		
	1.5	(83.337, -4.649, 7.695)		
TFSI	0	(95.427, -1.879, 9.533)		24.2
	0.95	(90.189, -10.042, 29.889)		
	1.25	(78.689, -16.415, 3.727)		

Table 3.4: $L^*a^*b^*$ values and respective colours at neutral and doped states

3.3.4 Nyquist plots and equivalent circuits

After our exhaustive investigation into counterion effect during electropolymerization on electrochromism, we now investigate similarly into effects of anion and porosity on electrochemical properties like impedance and capacitance of PTPE-4Cz's films. EIS measurements were done in the custom built electrochemical cell with an Ag wire as PRE. Potentials applied for EIS were ion insertion potentials from CV done just before the measurements(see figure 3.10a).

An important point to note here is the inconsistent CV of BF_4 based films. Since all experiments were done in an open environment, it is likely that films electropolymerized with BF_4 are very sensitive to environmetal conditions, since it is susceptible to side reactions like hydrolysis and decomposition to yield fluoride ions.

Thus BF_4's impedance spectra, as reported, may not be consistently reproducible. Similar problems were encountered with films of ClO_4 which leads us to suspect that electropoly-

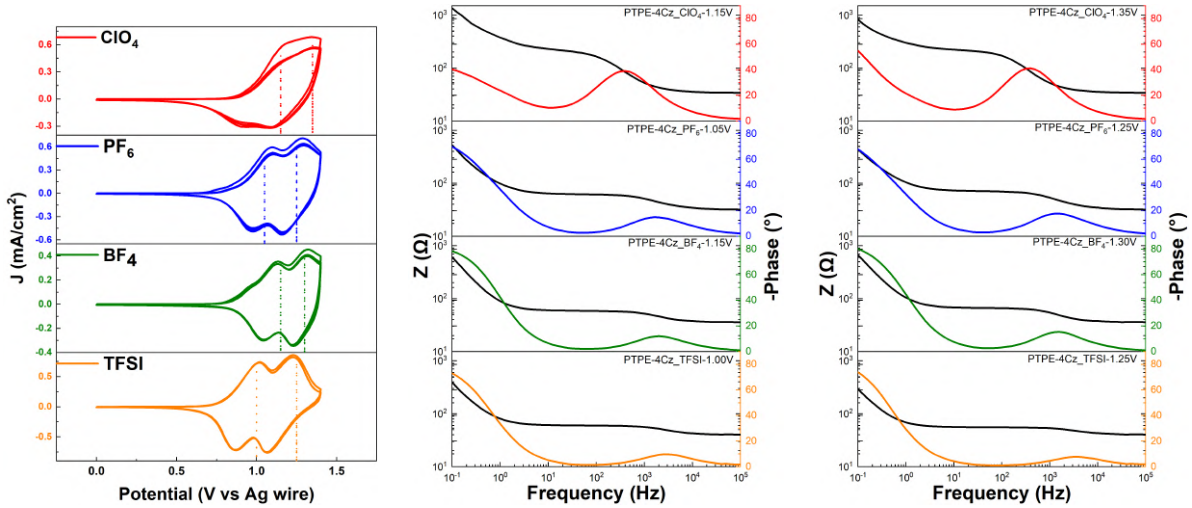

(a) CV taken before EIS measurements

(b) Bode plots at E_{ox_1}

(c) Bode plots at E_{ox_2}

Figure 3.10: CVs and corresponding Bode plots

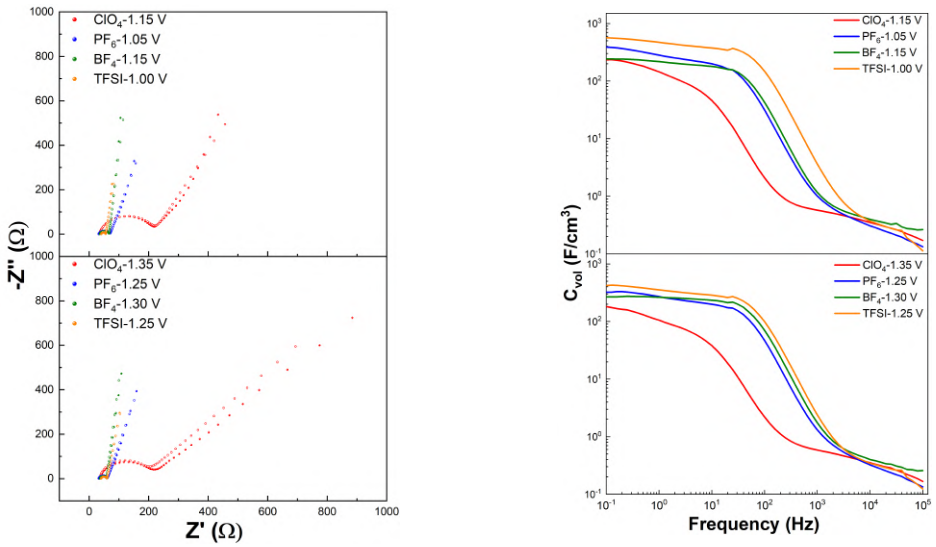

(a) Nyquist measured(filled) and fitted(hollow circles) plots

(b) Volumetric capacitance plots

Figure 3.11: Nyquist plots and volumetric capacitance

merization with these anions is sensitive to atmospheric moisture content resulting in an increase in charge transfer resistance (R_{CT}) in these films (figure 3.11a).

From the nyquist plots, a clear pattern, similar to our previous results is seen - Films made with larger anions show lower R_{CT}, reflected in the diameter of the semicircle at high

frequency regime. Since we already know that porosity is ion size dependent, we can also correlate R_{CT} values to porosity of the film. Equivalent circuit model was fitted with nyquist plots for all anions at first ion insertion potentials, where ClO_4, PF_6 and BF_4 follow circuit 3.12a whereas TFSI follows circuit 3.12b.

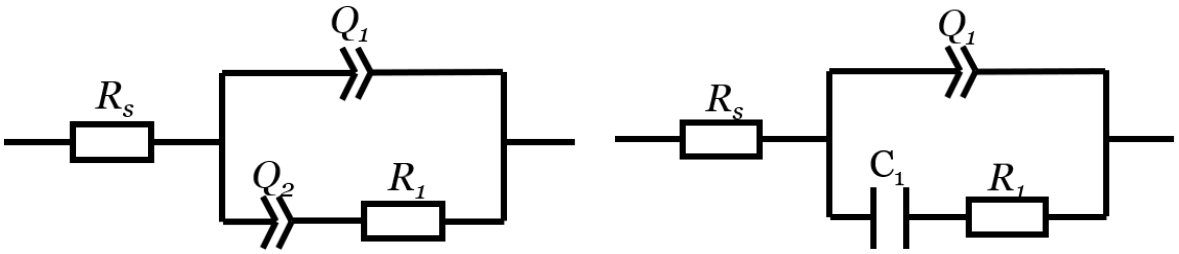

(a) Circuit for ClO_4, PF_6 and BF_4 (b) Circuit for TFSI

Figure 3.12: Equivalent circuit models for PTPE-4Cz

Anion	R_s (Ω)	C_1 (μF)	Q_1 ($mS.s^n$)	Q_2 ($mS.s^n$)	R_1 (Ω)
ClO_4	34.5	-	2.1	0.012	180.9
PF_6	32.1	-	3.7	0.015	39.1
BF_4	36	-	2.4	0.01	30.8
TFSI	41	3.5	5.4	-	14.4

Table 3.5: Equivalent circuit model fit parameters

The tail end of the nyquist plots tell us whether a material has capacitive properties or not, which can also be seen from the low frequency end of the bode plots. A higher phase angle indicates capacitive behaviour (90° for pure capacitor). PTPE-4Cz shows very high phase angle in the tail end of nyquist plots, implying capacitive behaviour. It can also be observed that ClO_4 film shows much lower phase angle, implying lower capacitive character. Volumetric capacitance plots show that the capacitance in low frequency regime increases with anion size, with TFSI based films showing much higher capacitance than other anions.

In the equivalent circuits, R_s is solution resistance, R_1 is ionic resistance (R_{ionic}), C_1 is bulk capacitance of the film (C_{bulk}) and Q_1 and Q_2 are constant phase elements (CPE). CPEs are in essence imperfect capacitors with some innate resistance. From the equivalent circuit fits (table 3.5), R_{ionic} follows the order TFSI (14.4 Ω)< BF_4 (30.8Ω)< PF_6 (39.1Ω)<

ClO_4 (180.9Ω) and TFSI shows a bulk capacitance value (C_{bulk}) of 3.5 μF. The low R_{ionic} value of TFSI suggests facile ion transport in TFSI based films, also reflected in the high contrast (ΔT (%)= ≈49%), colouration efficiency, and ΔE^*_{ab} values.

3.4 Topography Analysis

AFM is a scanning probe microscopy method that is used extensively for surface topography and calculating parameters like surface roughness in polymer thin films. We used AFM to probe the surface of PTPE-4Cz films made in all 4 anions for 10 cycles. From AFM images (figure 3.13), ClO_4 film shows very low porosity (lack of a globular surface visual). With increasing anion size, we observe a gradual increase in porosity. BF_4 films couldn't be imaged due to very high surface roughness.

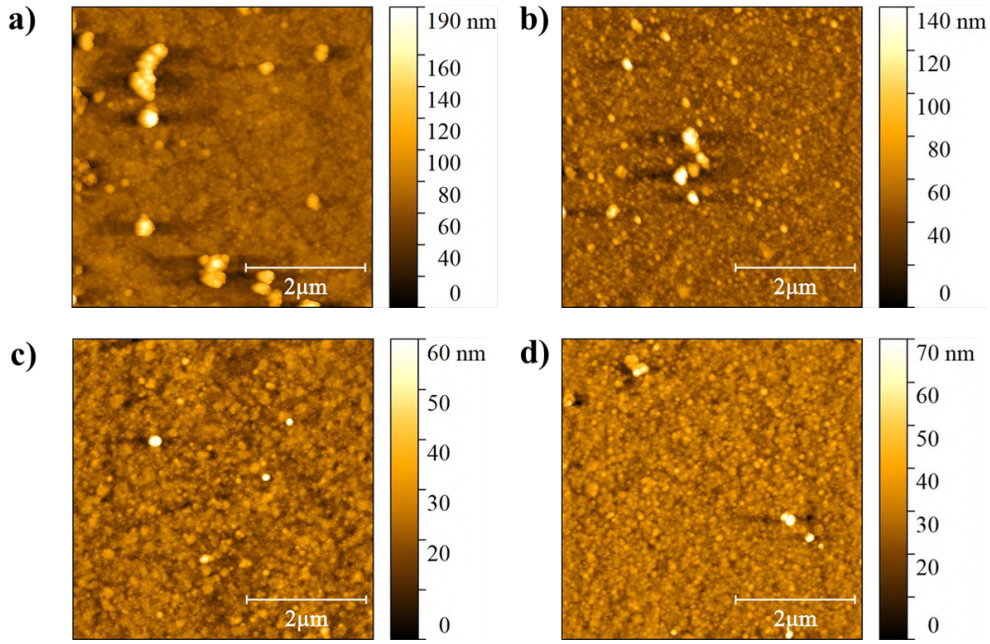

Figure 3.13: Tapping mode AFM images of electropolymerized PTPE-4Cz films with a) ClO_4 b) PF_6 c) OTf d) TFSI. The images were taken on a 5x5 μm^2 area. Note that Electropolymerization using BF_4 anion did not give a film with sufficient coverage and homogeneity.

From table 3.6, it is evident that larger anions result in smoother films. Given the increase in RMS roughness with decrease in anion size, it is highly probable that the very

high roughness observed in BF_4 films could be related to its low porosity. To support this claim, we must remember that during electropolymerization, the anions move from the polymer film to bulk electrolyte when the potential sweep direction is reversed. From previous discussions, we know that smaller anions result in films with lower porosity, where dedoping is inefficient resulting in a larger fraction of electrolyte bound to the films giving rise to higher roughness. Our previous results, together with AFM analysis points towards a clear dependence on porosity on the size of the counterion employed.

Polymer	Root mean square roughness (nm)
ClO_4	15.2
PF_6	10.5
OTf	4.4
TFSI	4.8

Table 3.6: RMS roughness values of PTPE-4Cz films

Although OTf films display very low surface roughness and good porosity, the surface coverage is quite inhomogenous (figure 3.13). As we have seen in section 3.2, OTf based films are very thin and do not show electrochromic behaviour. But films made using TFSI, a similar but larger anion that OTf, shows better porosity as well as the best performance in nearly all metrics we have tested, which leads us to the question of possible geometry dependence in electrochemical polymerization of CMPs. While this study does not answer this question, it appears as a possible future direction to step in.

3.5 Pseudocapacitor studies

Based on the highly capacitive behaviour we observed for TFSI based films in section 3.3.4, we decided to make a simple supercapacitor. However, given the actual low value of capacitance seen in the model fitting parameters, we do not expect high capacitance from these devices. Some steps involved in fabricating a supercapacitor are optimizing the substrate, electrolyte (liquid/ GPE) as well as a counter electrode.

3.5.1 Electrode material optimization

To begin with, we decided to use graphite based substrates as our electrode+ current collector. With this in mind we electropolymerized TPE-4Cz on various graphite based substrates- Toray carbon, IGS, graphite plates, flexible graphite plates, 1 mm and 6 mm graphite felt and RVC (figure 3.14).

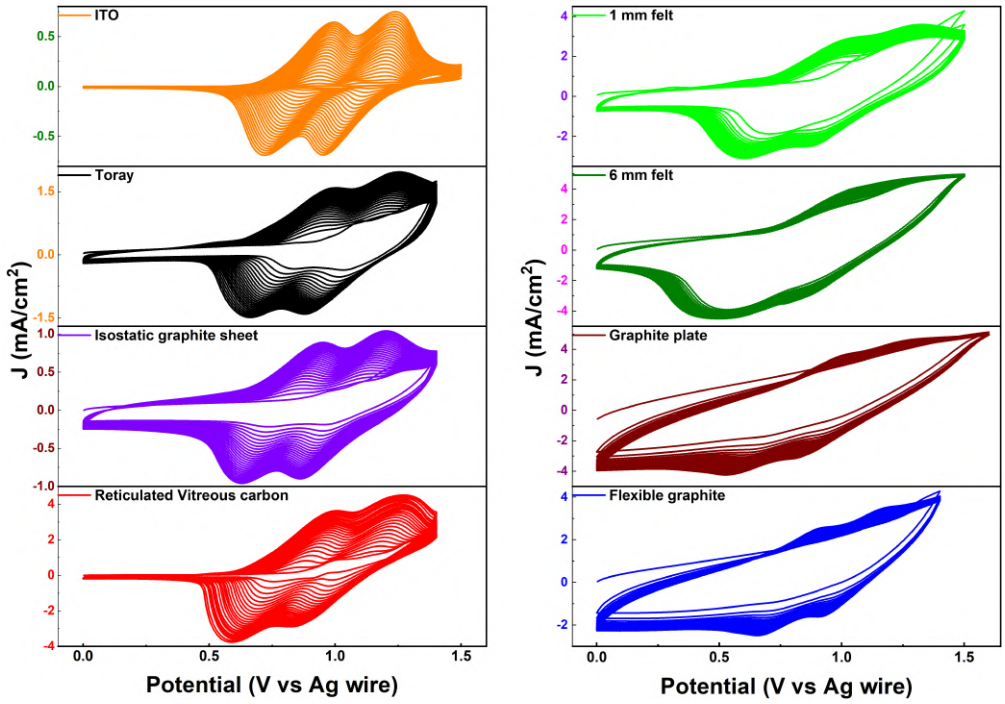

Figure 3.14: Polymerization CV profiles of PTPE-4Cz_TFSI on graphite substrates

From both polymerization and CV profiles (figures 3.14 and 3.15), we observe that the faradaic character of PTPE-4Cz is diminished in some substrates like graphite plate, flexible graphite sheets and 6 mm felt. To confirm if our films still showed capacitive behaviour, we decided to use EIS (figure 3.16). Toray carbon, IGS, 1 mm felt and RVC films showed similar capacitive behaviour at tail end of nyquist plots while other substrates showed very low phase angle in low frequency regime. Since RVC is very brittle, making a device using that would be considerably difficult for practical reasons. Hence we decided to try half cell studies on 1 mm felt, IGS and toray carbon. We also obtained SEM images of the films to confirm surface coverage of the polymer film (figure 3.17). The SEM images show slight delamination of PTPE-4Cz on graphite plate substrates. On RVC, the film formation is very smooth and can be observed throughout the substrate and not just on the surface.

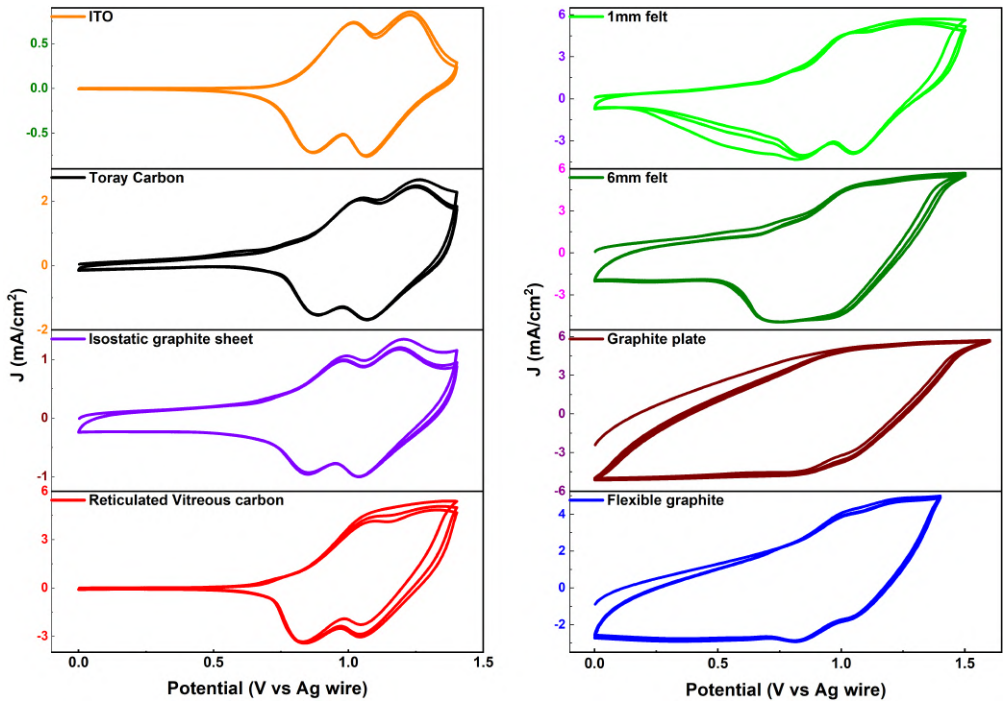

Figure 3.15: Pristine CV profiles of PTPE-4Cz_TFSI on graphite substrates

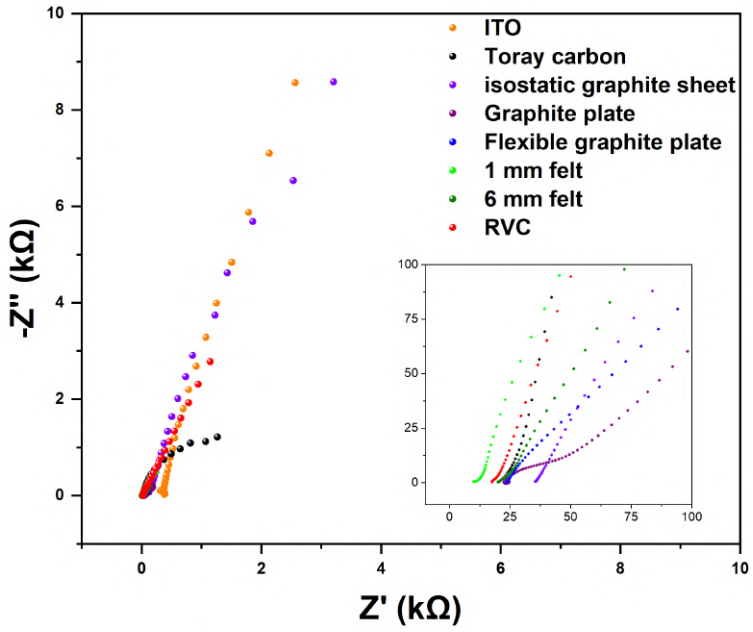

Figure 3.16: Nyquist plots of PTPE-4Cz_TFSI on graphite substrates

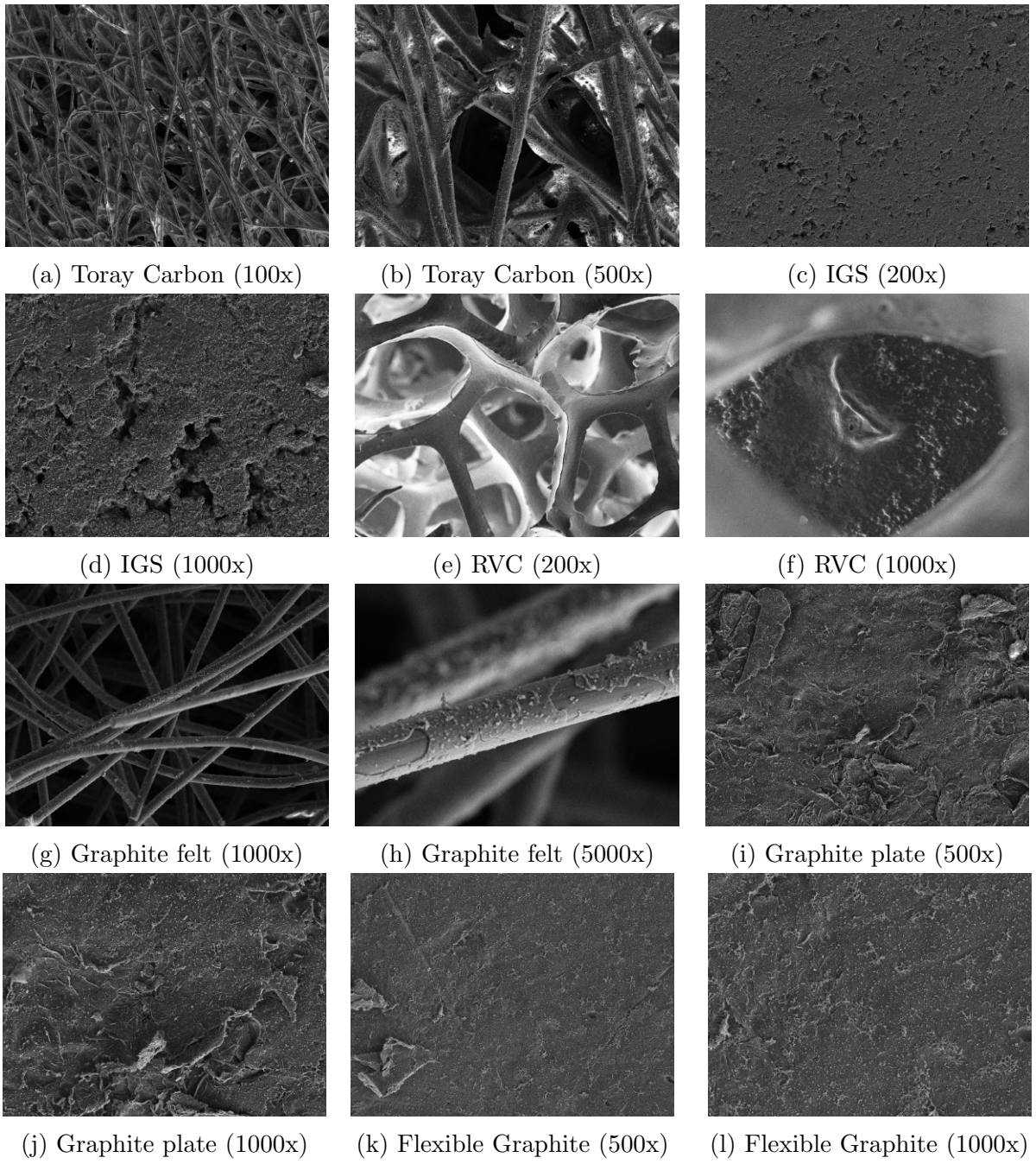

(a) Toray Carbon (100x) (b) Toray Carbon (500x) (c) IGS (200x)

(d) IGS (1000x) (e) RVC (200x) (f) RVC (1000x)

(g) Graphite felt (1000x) (h) Graphite felt (5000x) (i) Graphite plate (500x)

(j) Graphite plate (1000x) (k) Flexible Graphite (500x) (l) Flexible Graphite (1000x)

Figure 3.17: SEM images of PTPE-4Cz on graphite substrates.

3.5.2 Quest for cathode

Before starting half cell studies, we had to find a suitable counter electrode for our material. Initially, we tried using graphite substrates themselves as counter electrode. We also tried to

find if PTPE-4Cz could be used in a symmetric cell arrangement. Both of these yielded poor results (figure 3.18). We tried some conducting polymers (NDI-NDI-OD-OD, NDI-OD-TEG, PEDOT: PSS, PANI, PANI/AC composite) as well as some n-type molecules (DPP-Hex-CN4) and activated carbon. We optimized the cathode using simple CV profiles in two electrode configuration (see figure 3.18).

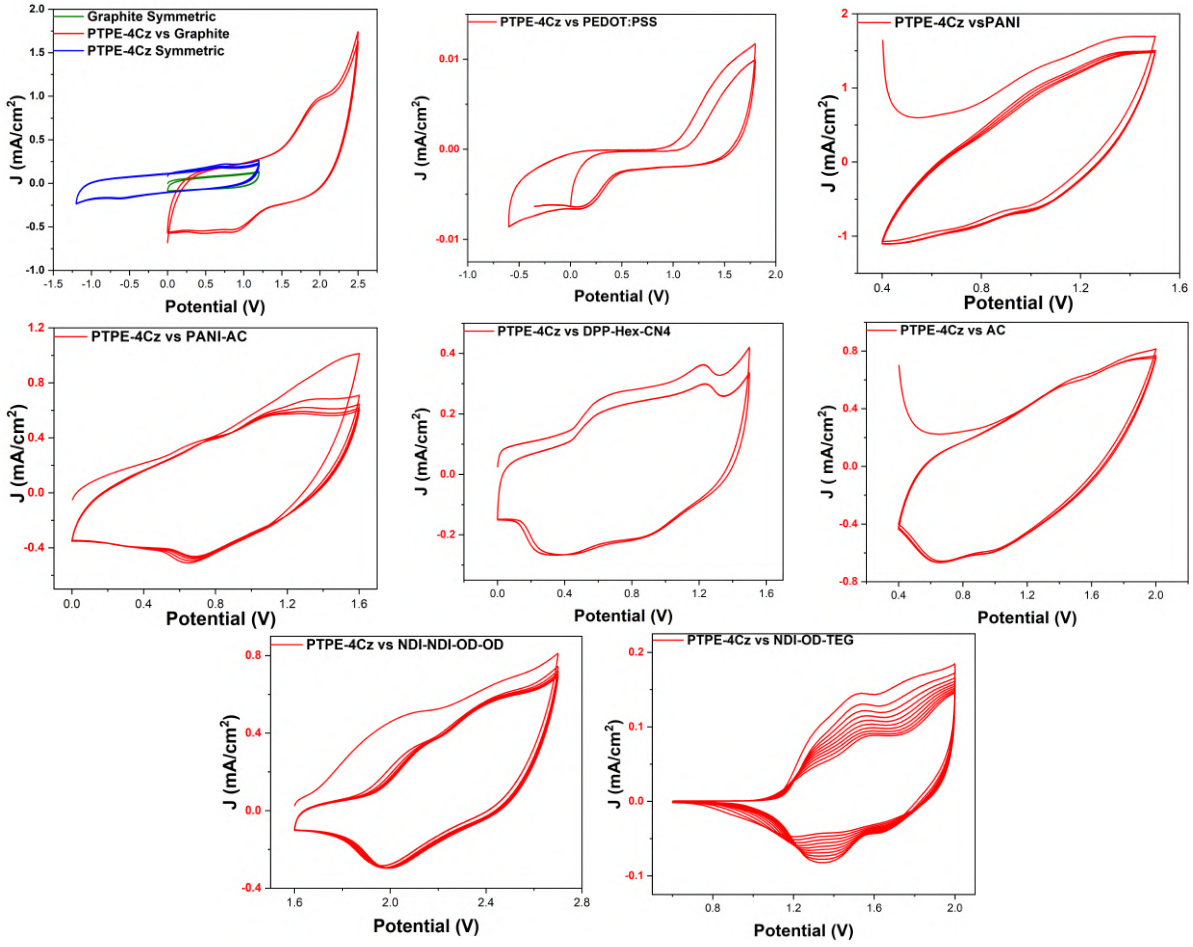

Figure 3.18: CV of PTPE-4Cz with other counter electrodes

As it can be seen, PEDOT: PSS gave very poor results while PANI, PANI/AC electrodes CV do not have very distinguishable peaks. In DPP-Hex CN4's case, although our CV looks very good, unfortunately the counter is soluble in ACN which makes it unsuitable for solid/liquid electrolyte based devices. With NDI-OD-TEG, the CV is unstable over extended cycling while in NDI-NDI-OD-OD's case, the potential window is not suitable. Finally, we were left with AC as a viable option with mildly distinguishable peaks. We decided to test two electrode studies of PTPE-4Cz vs AC on IGS, toray carbon and 1 mm felt. We were

not able to get good CVs with 1 mm felt while toray carbon had huge equivalent series resistance in GCDs hence we opted for IGS as the most stable electrode material and AC as the cathode.

3.5.3 Device fabrication- GPE salt optimization

With AC as cathode and PTPE-4Cz as anode, we fabricated a simple solid state supercapacitor with a GPE loaded into a well created using double side adhesive between the IGS electrodes. We tested several different salts for GPE - $LiClO_4$, $TBAPF_6$, KPF_6, $TEABF_4$, NaOTf and LiTFSI. Since we are heating our gel solution at 65 °C, we couldn't get a stable GPE of $LiPF_6$ as its stability window is limited to < 55 °C. The mass loading of AC was maintained at 1 mg/cm^2 for all the devices (except KPF_6 which was 1.5 mg/cm^2). The scanrate profiles and GCD curves of the device in various GPEs is given in figure 3.19.

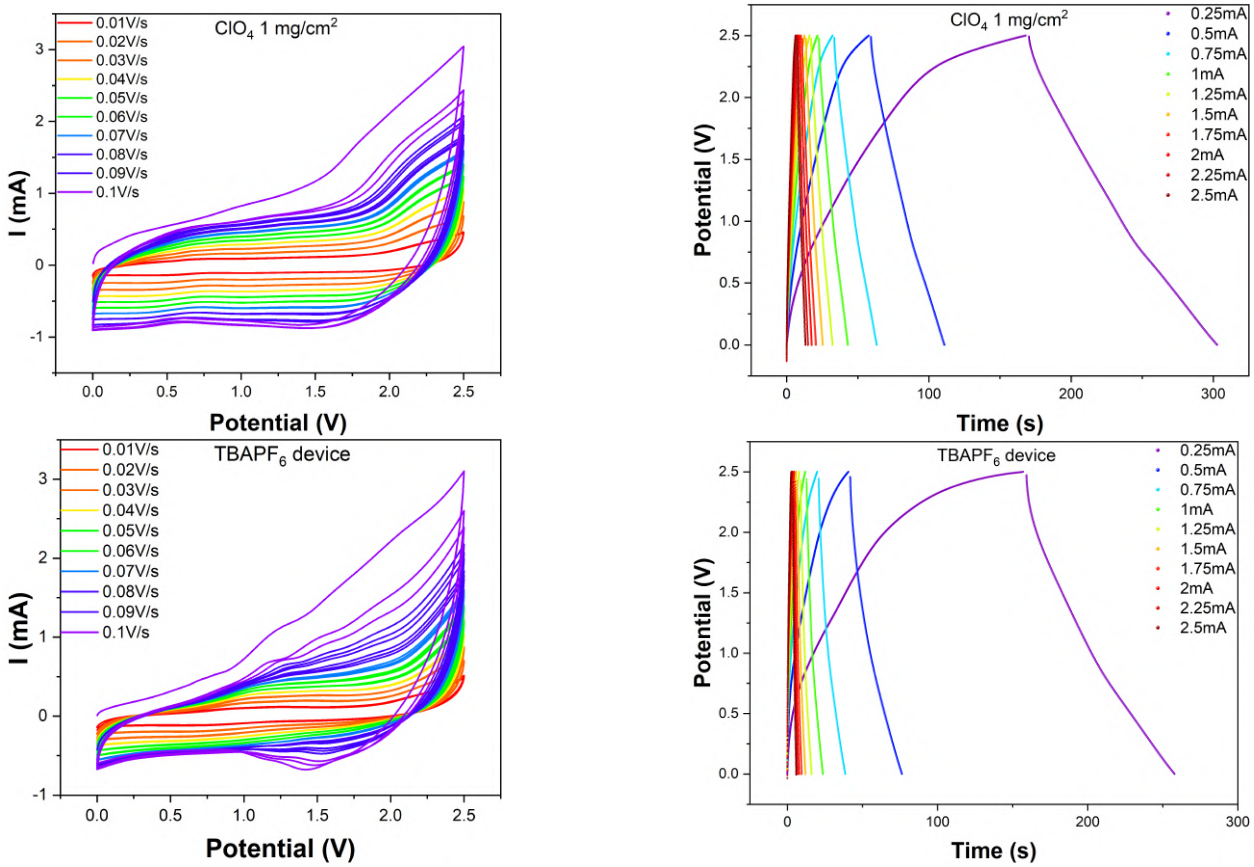

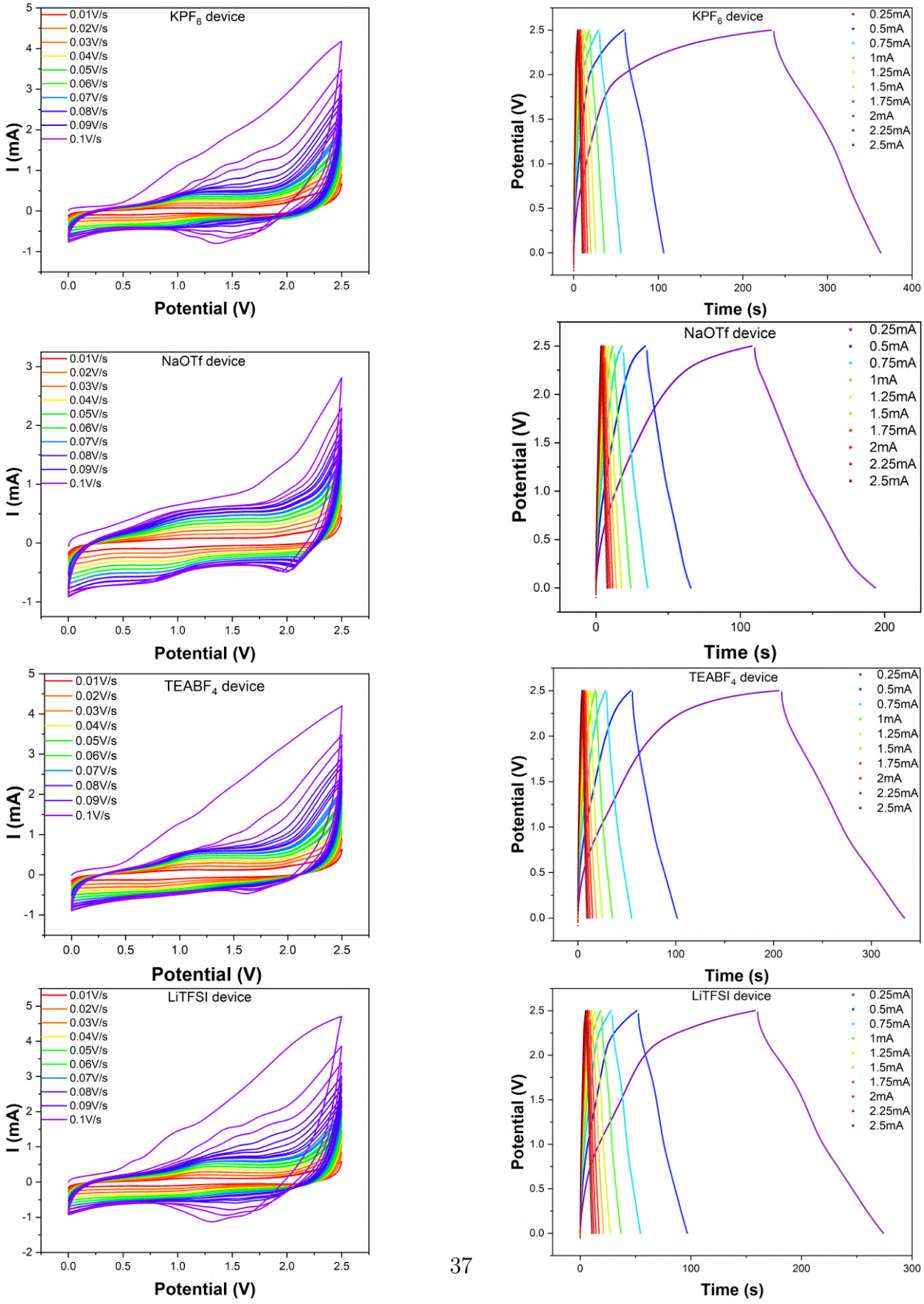

Figure 3.19: Scanrate and GCD curves for all GPE variants

Among them, ClO_4 based cells showed the best GCD behaviour (KPF_6 showed higher C_s but lower E.D) and we decided to use it for further studies. To ensure whether PTPE-4Cz is actually functioning as a WE, we also used two reference cells, one with just PTPE-4Cz vs IGS and one AC vs IGS in ClO_4 based gel. the reference cell scanrate profile can be seen in figure 3.20. From their CV profiles it is clear that our WE is functional and our device CVs are not just because of AC and IGS. $C_o.E$, C_s, E.D and P.D were calculated for all the cells using equations eqs. (2.7) to (2.11) (Table tables 3.7 to 3.11).

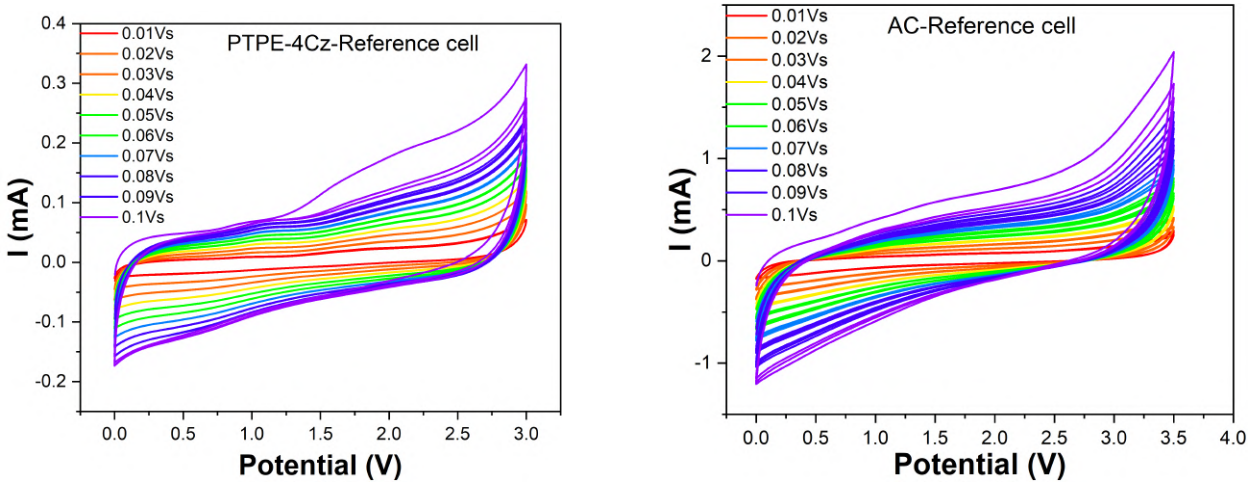

Figure 3.20: Scanrate profile of reference cells

Device	C_o.E (%) at current I (mA)									
	0.25	0.5	0.75	1	1.25	1.5	1.75	2	2.25	2.5
$TBAClO_4$	78.8	89.5	92.4	93.7	93.7	93.7	96	94.4	95.8	96.5
$TBAPF_6$	62.8	84.5	88.9	91	92.6	93.2	92.7	93.6	93.1	93.1
KPF_6	54	76.8	85	88.7	90	92.7	93.6	93.4	94	96
TBAOTf	77.6	88.7	92.7	94.4	94.7	96.4	95.5	95.2	96	95.5
$TEABF_4$	61.1	84.4	89.8	92.4	93.3	94.6	95.1	94.8	95.6	94.7
LiTFSI	72	86	90.7	91.9	93.9	94.2	94.8	95.6	95.4	96.8

Table 3.7: Coulombic efficiencies of all GPE variant devices

Device	ESR (Ω) at current I (mA)									
	0.25	0.5	0.75	1	1.25	1.5	1.75	2m	2.25	2.5
$TBAClO_4$	29.32	24.42	25.24	22.28	18.56	16.89	15.87	13.27	14.11	10.99
$TBAPF_6$	112.32	86.68	76.5	64.09	56.65	51.27	47.43	42.57	36.89	34.92
KPF_6	65.92	58	53.31	49.44	45.9	41.1	40.46	38.91	35.95	36.26
TBAOTf	98.88	96.44	92.37	83.93	81.79	63.3	70.8	68.21	62.39	57.86
$TEABF_4$	58.6	37.86	32.15	24.72	21.98	17.91	14.3	14.92	10.44	7.94
LiTFSI	78.16	73.26	67.96	64.7	63.73	60.36	58.42	57.37	55.61	54.81

Table 3.8: ESR values of all GPE variant devices

Device	Active mass	C_s (Fg^{-1}) at current I (mA)									
	mg	0.25	0.5	0.75	1	1.25	1.5	1.75	2	2.25	2.5
$TBAClO_4$	3.08	8.60	6.71	5.83	5.28	4.90	4.60	4.37	4.21	4.04	3.93
$TBAPF_6$	3.41	5.78	4.03	3.11	2.53	2.15	1.89	1.71	1.58	1.50	1.43
KPF_6	2.08	12.14	8.78	7.27	6.38	5.77	5.38	5.03	4.77	4.58	4.38
TBAOTf	3.63	4.62	3.35	2.78	2.48	2.27	2.14	2.03	1.95	1.90	1.85
$TEABF_4$	3.88	6.47	4.72	3.95	3.41	3.01	2.72	2.50	2.33	2.20	2.10
LiTFSI	3.9	5.83	4.53	3.90	3.51	3.23	3.02	2.84	2.69	2.58	2.47

Table 3.9: Specific Capacitance of all GPE variant devices

Device	E.D (Wh/Kg) at current I (mA)									
	0.25	0.5	0.75	1	1.25	1.5	1.75	2	2.25	2.5
$TBAClO_4$	7.47	5.83	5.06	4.59	4.26	4.00	3.80	3.65	3.51	3.42
$TBAPF_6$	5.02	3.50	2.70	2.20	1.87	1.64	1.49	1.38	1.31	1.25
KPF_6	7.41	5.36	4.44	3.89	3.53	3.28	3.07	2.91	2.80	2.67
TBAOTf	4.01	2.91	2.42	2.16	1.97	1.86	1.77	1.69	1.65	1.61
$TEABF_4$	5.62	4.10	3.43	2.97	2.62	2.37	2.18	2.03	1.91	1.83
LiTFSI	5.07	3.93	3.39	3.05	2.81	2.62	2.47	2.34	2.24	2.15

Table 3.10: Energy Density of all GOE variant devices

Device	P.D (W/Kg) at current I (mA)									
	0.25	0.5	0.75	1	1.25	1.5	1.75	2	2.25	2.5
$TBAClO_4$	203.05	406.11	609.16	812.22	1015.27	1218.32	1421.38	1624.43	1827.49	2030.54
$TBAPF_6$	183.28	366.57	549.85	733.14	916.42	1099.71	1282.99	1466.28	1649.56	1832.84
KPF_6	211.15	422.30	633.45	844.59	1055.74	1266.89	1478.04	1689.19	1900.34	2111.49
TBAOTf	172.37	344.73	517.10	689.46	861.83	1034.20	1206.56	1378.93	1551.30	1723.66
$TEABF_4$	161.08	322.16	483.25	644.33	805.41	966.49	1127.58	1288.66	1449.74	1610.82
LiTFSI	160.26	320.51	480.77	641.03	801.28	961.54	1121.79	1282.05	1442.31	1602.56

Table 3.11: Power Density of all GPE variant devices

3.5.4 Device fabrication- AC mass loading optimization

With the salt in GPE optimized, we then began with optimization of the CE mass loading, by varying it from 0.5 to 2.5 mg/cm^2. Dead weight on CE was observed above mass loading of 1.5 mg/cm^2. Scanrate profiles and GCD curves of the devices tested are given below (figure 3.21), 1 mg/cm^2 is omitted (refer figure 3.19).

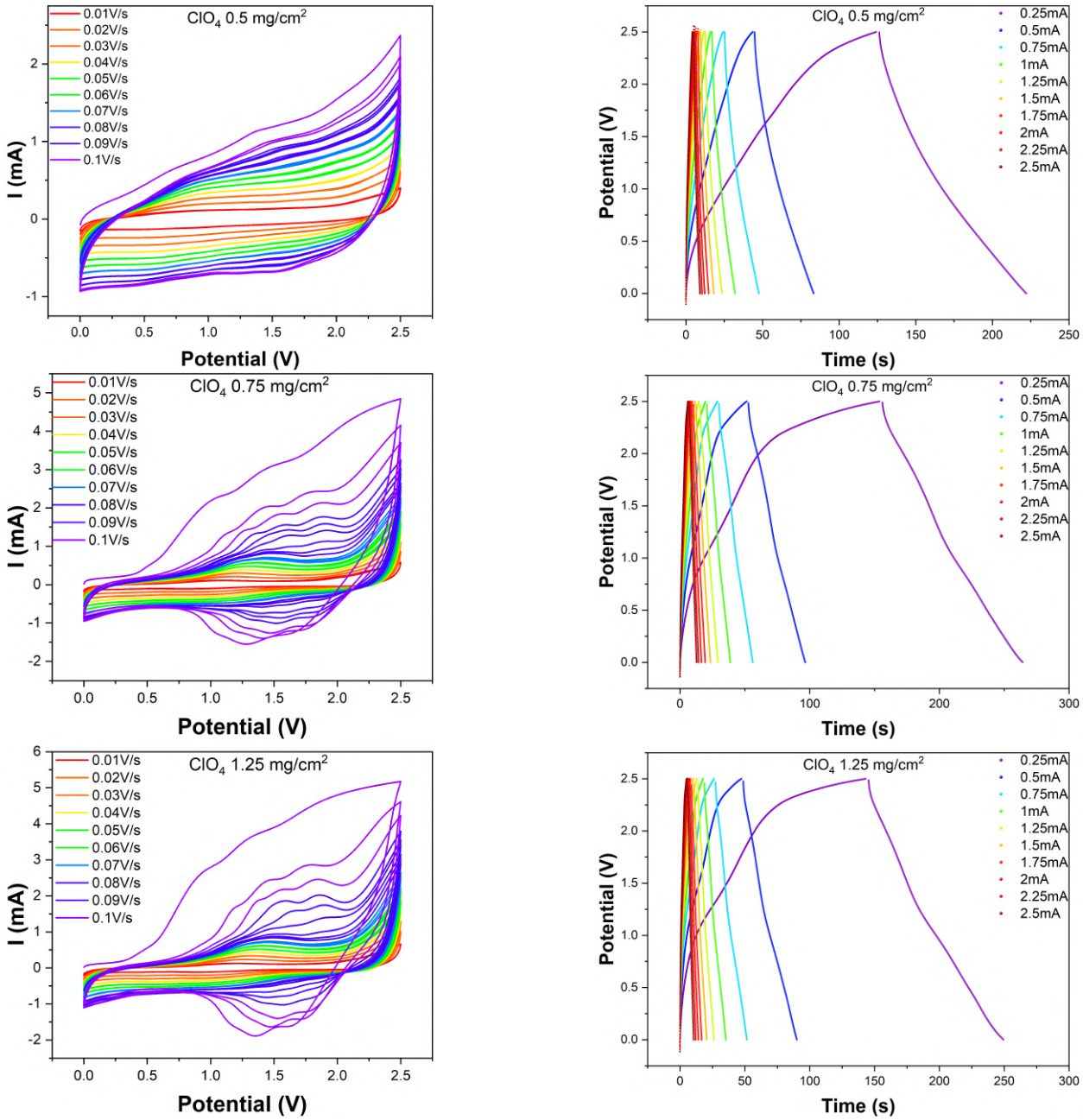

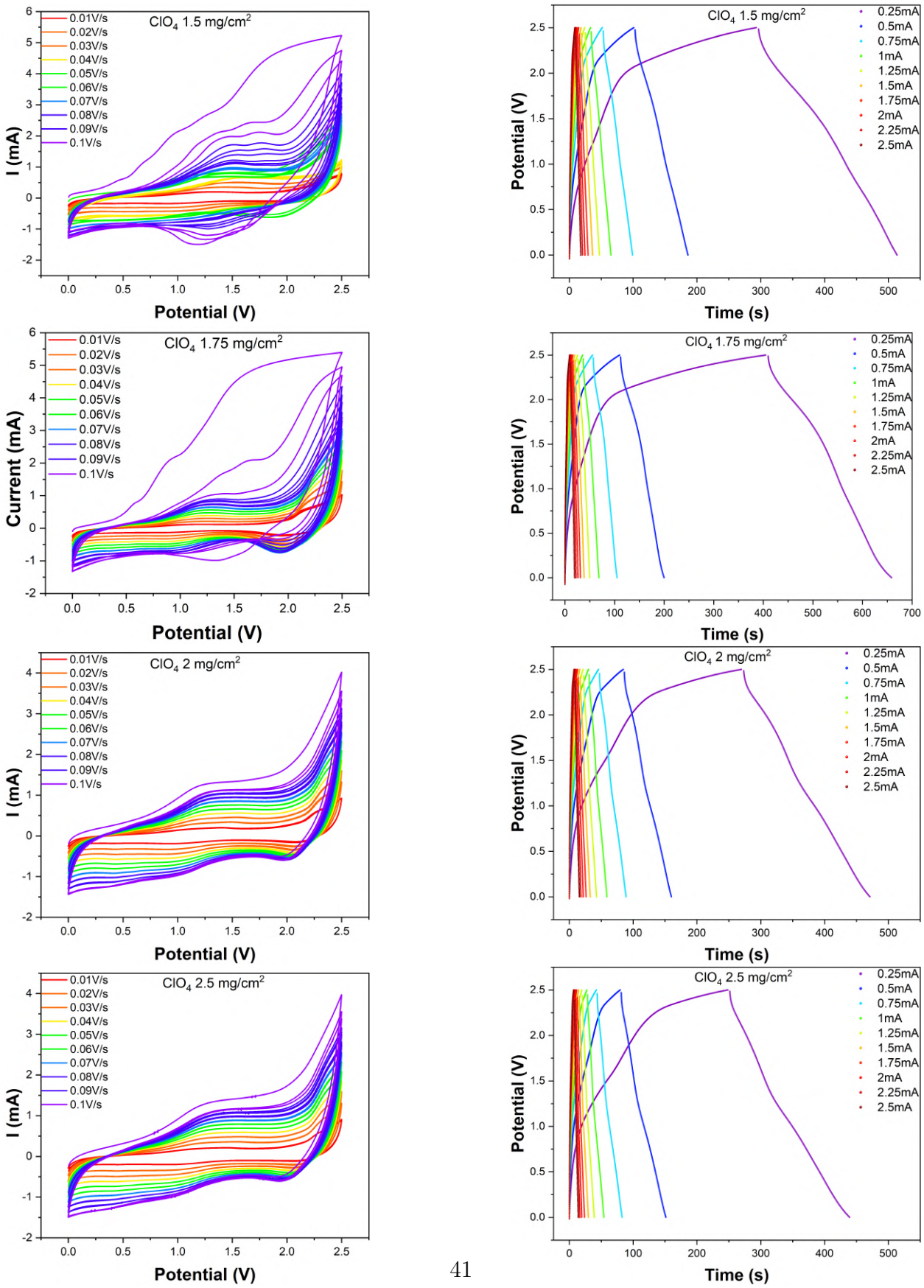

Figure 3.21: Scanrate and GCD curves for all AC mass variants

Device	C_o.E (%) at current I (mA)									
mg/cm^2 of AC	0.25	0.5	0.75	1	1.25	1.5	1.75	2	2.25	2.5
0.5	77.2	88.6	92	93.6	94.7	95.6	95.3	95.7	96.3	95.3
0.75	70.3	85.2	90	92.1	93.6	94.3	95.3	95	95.3	96.6
1	78.8	89.5	92.4	93.7	93.7	93.7	96	94.4	95.8	96.5
1.25	72.6	87.3	91.6	93.6	94.7	95.6	95.1	95.6	95.8	95.4
1.5	74.1	82.1	89.1	92.1	97.6	94.6	95.4	95.6	96.7	96.5
1.75	61.4	79.4	85.7	88.8	91.1	91.9	93.6	94.1	94.6	95.5
2	73.3	87.3	91.2	93.2	94.4	95.1	95.8	95.8	96.4	96
2.5	75.7	88.1	92.2	93.6	94.8	95.4	91.4	96.6	96.5	97.1

Table 3.12: Coulombic efficiencies of all CE mass variants

Device	ESR (Ω) at current I (mA)									
mg/cm^2 of AC	0.25	0.5	0.75	1	1.25	1.5	1.75	2	2.25	2.5
0.5	12.2	6.72	2.85	1.53	6.83	10.37	15.34	16.32	21.83	22.09
0.75	43.96	36.02	32.15	28.08	26.37	21.97	19.88	19.38	18.31	13.92
1	29.32	24.42	25.24	22.28	18.56	16.89	15.87	13.27	14.11	10.99
1.25	56.16	47	45.57	40.29	38.09	34.39	34.53	29.91	28.75	29.42
1.5	63.48	48.84	47.61	47	45.17	44.15	42.72	41.2	40.01	40.29
1.75	45.2	42.74	42.73	41.81	39.8	40.08	38.02	36.16	360.8	36.01
2	59.84	62.26	59.82	57.38	56.16	55.14	52.67	51.88	52.35	51.88
2.5	59.84	58	54.53	52.8	51.03	49.44	47.43	47.3	46.25	45.29

Table 3.13: ESR values of all CE mass variants

Device	Active mass	C_s (Fg^{-1}) at current I (mA)									
mg/cm^2 of AC	mg	0.25	0.5	0.75	1	1.25	1.5	1.75	2	2.25	2.5
0.5	2.85	6.74	5.42	4.71	4.23	3.87	3.58	3.35	3.15	3.02	2.87
0.75	3.06	7.07	5.73	5.10	4.74	4.47	4.27	4.12	3.99	3.88	3.83
1	3.08	8.60	6.72	5.83	5.28	4.91	4.61	4.38	4.21	4.05	3.94
1.25	4.1	5.08	4.04	3.54	3.24	3.00	2.81	2.64	2.53	2.42	2.32
1.5	4.14	10.49	8.03	6.68	5.92	5.38	4.98	4.68	4.42	4.22	4.02
1.75	4.92	10.11	7.13	5.85	5.17	4.73	4.40	4.17	4.00	3.83	3.70
2	4.34	9.13	6.82	5.79	5.15	4.65	4.27	3.98	3.73	4.75	3.32
2.5	5.62	6.69	5.00	4.17	3.65	3.29	3.00	2.64	2.58	2.42	2.30

Table 3.14: Specific Capacitance of all CE mass variants

Tables tables 3.12 to 3.16 contain C_o.E, ESR, C_s, E.D and P.D values calculated for all CE mass variants. From these, the optimal AC mass loading was found to be 1.5 mg/cm^2.

Device	E.D (Wh/Kg) at current I (mA)									
mg/cm^2 of AC	0.25	0.5	0.75	1	1.25	1.5	1.75	2	2.25	2.5
0.5	5.85	4.71	4.09	3.67	3.36	3.11	2.91	2.73	2.62	2.49
0.75	6.14	4.97	4.43	4.11	3.88	3.71	3.58	3.46	3.37	3.32
1	7.47	5.83	5.06	4.59	4.26	4.00	3.80	3.65	3.51	3.42
1.25	4.41	3.50	3.07	2.81	2.60	2.44	2.29	2.20	2.10	2.01
1.5	9.11	6.97	5.80	5.14	4.67	4.32	4.06	3.84	3.66	3.49
1.75	8.78	6.19	5.08	4.49	4.11	3.82	3.62	3.47	3.33	3.21
2	7.93	5.92	5.02	4.47	4.03	3.71	3.45	3.24	4.12	2.88
2.5	5.81	4.34	3.62	3.17	2.85	2.61	2.29	2.24	2.10	1.99

Table 3.15: Energy Density of all CE mass variants

Device	P.D (W/Kg) at current I (mA)									
mg/cm^2 of AC	0.25	0.5	0.75	1	1.25	1.5	1.75	2	2.25	2.5
0.5	219.61	439.21	658.82	878.43	1098.03	1317.64	1537.25	1756.85	1976.46	2196.06
0.75	204.05	408.10	612.14	816.19	1020.24	1224.29	1428.34	1632.39	1836.43	2040.48
1	203.05	406.11	609.16	812.22	1015.27	1218.32	1421.38	1624.43	1827.49	2030.54
1.25	152.48	304.95	457.43	609.90	762.38	914.86	1067.33	1219.81	1372.29	1524.76
1.5	151.04	302.08	453.12	604.16	755.20	906.23	1057.27	1208.31	1359.35	1510.39
1.75	127.03	254.07	381.10	508.13	635.16	762.20	889.23	1016.26	1143.29	1270.33
2	144.18	288.35	432.53	576.70	720.88	865.05	1009.23	1153.40	1297.58	1441.75
2.5	111.25	222.50	333.75	445.00	556.25	667.50	778.75	890.00	1001.25	1112.50

Table 3.16: Power Density of all CE mass variants

With the CE mass loading optimized, we varied the salt : PMMA ratio in ClO_4 based GPE which resulted in almost double the discharge time. The two gels we used had the following salt : PMMA ratios- 0.45 : 1.05 and 0.5 : 0.5 . Mass loading of AC was the optimized 1.5 mg/cm^2. For future studies, we plan to increase the polymer mass loading considering the actual mass loading of polymer is quite lower than it initially seems as a large part of the mass observed for the film is contributed by the salt accompanying the film. Figure 3.22 shows the difference in discharge times between devices made with the two gels. Table 3.17 gives the calculated values of various quantities for the higher concentration electrolyte device.

At this stage, we have achieved a supercapacitor using PTPE-4Czelectropolymerized in LiTFSI electrolyte with max capacitance of 18.27 F g^{-1} recorded at 0.25 mA. We believe the low capacitance is likely due to both PTPE-4Cznot being able to store enough charge

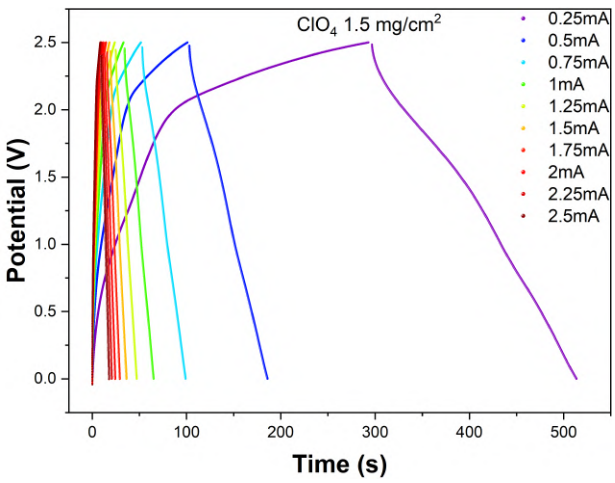

(a) Device with 0.45:1.05 salt:PMMA

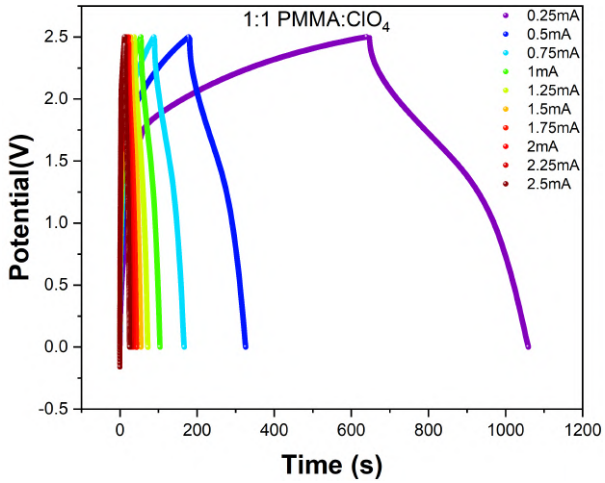

(b) Device with 0.5:0.5 salt:PMMA

Figure 3.22: GCD curves for salt:PMMA ratio enhancement

Quantity	Current (mA)									
	0.25	0.5	0.75	1	1.25	1.5	1.75	2	2.25	2.5
C_o.E (%)	64.33	81.50	86.70	89.50	91.10	92.20	93.00	93.40	94.20	94.70
ESR (Ω)	30.52	32.36	31.75	31.64	30.77	29.91	28.95	28.23	27.27	26.37
C_s (F g^{-1})	18.27	12.90	10.21	8.62	7.58	6.84	6.30	5.87	5.53	5.25
E.D (Wh kg^{-1})	15.86	11.20	8.86	7.49	6.58	5.94	5.46	5.09	4.80	4.56
P.D (W kg^{-1})	138.58	277.16	415.74	554.32	692.90	831.49	970.07	1108.65	1247.23	1385.81

Table 3.17: Quantities calculated for 0.5:0.5 ClO_4:PMMA

as well as our device CVs not being quasi-rectangular enough, a feature seen in many pseudocapacitors, pointing towards requiring a better cathode against PTPE-4Cz.

Chapter 4

Conclusions

The present study elucidates the drastic effect of counterion size on the electrochemical properties of electrochemically polymerized CMPs. We conducted a systematic study of anion transport in a p type CMP PTPE-4Cz when electrosynthesized using counterions of various sizes, resulting in films with varying porosity. Considering no similar studies done with CMPs, we explored several probabilities ranging from similarly sized pores to varying pore size in these films as well as anion-polymer backbone interactions through spectro-electrochemical techniques.

Intuitively, smaller anions should be able to dope to a higher extent into the bulk polymer due to a size advantage and give rise to higher porosity. However, our results suggest the opposite, linking the dedoping process to the formation of the pores leading to higher porosity with increase in anion size. Increase in anions' size also shows an increase in capacitive behaviour of the films as well as lower charge transfer resistance. We also notice stark contrast in the elctrochromic behaviour of PTPE-4Cz depending on the anion used, with larger anions showing much higher contrast (4-5x of smaller anions) as well as far better switching kinetics. Our results are further strngthened by topography images from AFM showing higher porosity and lower RMS roughness in films made with larger anions. Interestingly, OTf based films are very smooth and porous but have inhomogenous coverage while TFSI, an even larger anion shows similar porosity but has much better surface coverage, hinting towards a possible dependence on ion geometry in the electropolymerization of CMPs. We also demostrate a simple supercapacitor based on PTPE-4Cz.

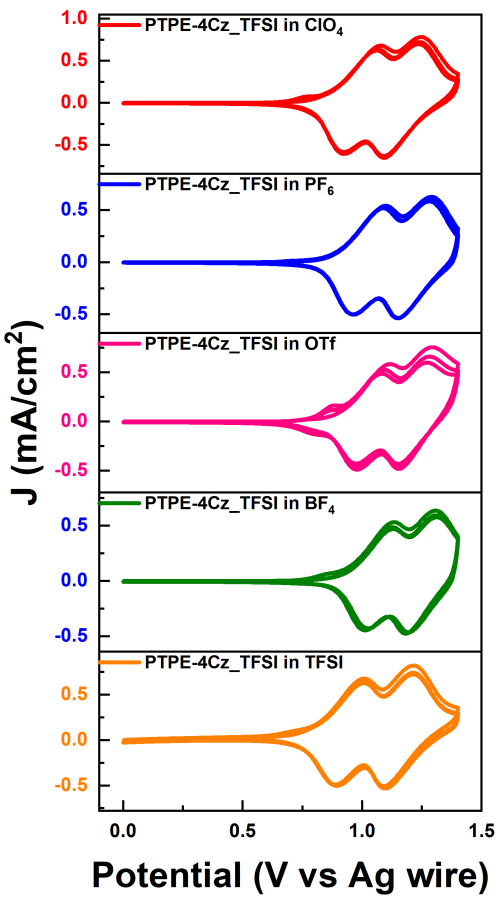

Figure 4.1: CV of PTPE-4Cz_TFSI in other electrolytes

For future directions, we believe there may be an ion size dependent degree of cross linking aspect to CMPs not yet explored. Since the exact mechanism of electropolymerization in CMPs is still not answered, we hope to be able to come up with an ion size dependent mechanism to explain the connectivity in PTPE-4Cz. Another aspect to strengthen our claims on ion size dependent porosity is ion agnostic behaviour post electrochemical polymerization. Figure 4.1 shows that the CV of TFSI based films in other electrolytes is nearly identical to CV in LiTFSI. This gives some credence to the ion size dependence during electropolymerization as it suggests the probability of counterion-polymer backbone interactions to be negligible, which makes sense as PTPE-4Cz does not have side chains to facilitate such interactions. Therefore anion doping post electrosynthesis must be agnostic towards pore size when films are made with a single anion. This preliminary hypothesis can be tested by spectro-electrochemistry experiments of TFSI based films in other electrolytes, which should give us nearly identical results if the hypothesis is true. With this we believe this study lays the groundwork towards mechanistic investigations into ion size dependent electrochemical polymerization of CMPs.

Bibliography

(1) Wang, X.; Smela, E. In *Smart Structures and Materials 2005: Electroactive Polymer Actuators and Devices (EAPAD)*, 2005; Vol. 5759, pp 414–422.

(2) Wang, X.; Shapiro, B.; Smela, E. *The Journal of Physical Chemistry C* **2009**, *113*, 382–401.

(3) Tropp, J.; Meli, D.; Wu, R.; Xu, B.; Hunt, S.; Azoulay, J.; Paulsen, B.; Rivnay, J. **2022**.

(4) Zhang, L.; Andrew, T. L. *Advanced Materials Interfaces* **2017**, *4*, 1700873.

(5) Wang, X.; Smela, E. *The Journal of Physical Chemistry C* **2009**, *113*, 369–381.

(6) Grzeszczuk, M.; Żabińska-Olszak, G. *Journal of Electroanalytical Chemistry* **1993**, *359*, 161–174.

(7) Seki, Y.; Takahashi, M.; Takashiri, M. *RSC advances* **2019**, *9*, 15957–15965.

(8) Ohayon, D.; Flagg, L. Q.; Giugni, A.; Wustoni, S.; Li, R.; Hidalgo Castillo, T. C.; Emwas, A.-H.; Sheelamanthula, R.; McCulloch, I.; Richter, L. J., et al. *ACS Materials Au* **2023**.

(9) Lee, J.-S. M.; Cooper, A. I. *Chemical reviews* **2020**, *120*, 2171–2214.

(10) Ma, H.; Chen, Y.; Li, X.; Li, B. *Advanced Functional Materials* **2021**, *31*, 2101861.

(11) Jiang, J.-X.; Su, F.; Trewin, A.; Wood, C. D.; Campbell, N. L.; Niu, H.; Dickinson, C.; Ganin, A. Y.; Rosseinsky, M. J.; Khimyak, Y. Z., et al. *Angewandte Chemie International Edition* **2007**, *46*, 8574–8578.

(12) Gu, C.; Huang, N.; Chen, Y.; Qin, L.; Xu, H.; Zhang, S.; Li, F.; Ma, Y.; Jiang, D. *Angewandte Chemie* **2015**, *127*, 13798–13802.

(13) Guo, D.; Li, X.; Wahyudi, W.; Li, C.; Emwas, A.-H.; Hedhili, M. N.; Li, Y.; Lai, Z. *ACS nano* **2020**, *14*, 17163–17173.

(14) Samy, M. M.; Mohamed, M. G.; Kuo, S.-W. *Polymers* **2023**, *15*, 1095.

(15) Mohamed, M. G.; Mansoure, T. H.; Samy, M. M.; Takashi, Y.; Mohammed, A. A.; Ahamad, T.; Alshehri, S. M.; Kim, J.; Matsagar, B. M.; Wu, K. C.-W., et al. *Molecules* **2022**, *27*, 2025.

(16) Amin, K.; Ashraf, N.; Mao, L.; Faul, C. F.; Wei, Z. *Nano Energy* **2021**, *85*, 105958.

(17) Wang, H.-g.; Li, Q.; Wu, Q.; Si, Z.; Lv, X.; Liang, X.; Wang, H.; Sun, L.; Shi, W.; Song, S. *Advanced Energy Materials* **2021**, *11*, 2100381.

(18) Zhang, Y.; Sun, Q.; Li, Z.; Zhi, Y.; Li, H.; Li, Z.; Xia, H.; Liu, X. *Materials Chemistry Frontiers* **2020**, *4*, 3040–3046.

(19) Hsiao, S.-H.; Hsueh, J.-C. *Journal of Electroanalytical Chemistry* **2015**, *758*, 100–110.

(20) Hu, B.; Li, J.; Wang, Y.; Hu, X.; Shi, Y.; Jin, L. *Electrochimica Acta* **2022**, *436*, 141450.

(21) Rendón-Enrıéquez, I.; Palma-Cando, A.; Körber, F.; Niebisch, F.; Forster, M.; Tausch, M. W.; Scherf, U. *Molecules* **2023**, *28*, 883.

(22) Lee, J.-S. M.; Wu, T.-H.; Alston, B. M.; Briggs, M. E.; Hasell, T.; Hu, C.-C.; Cooper, A. I. *Journal of Materials Chemistry A* **2016**, *4*, 7665–7673.

(23) Chen, X.; Tung, W.-Y.; Yang, K.; Chen, Y.-M.; Liu, K.; Cheng, C.-F.; Zhu, Y. *ACS Applied Polymer Materials* **2019**, *1*, 1634–1640.

(24) Li, Y.; Sun, X.; Zhang, X.; Zhang, D.; Xia, H.; Zhou, J.; Ahmad, N.; Leng, X.; Yang, S.; Zhang, Y., et al. *Journal of Materials Chemistry C* **2020**, *8*, 2676–2681.

(25) Palma-Cando, A.; Woitassek, D.; Brunklaus, G.; Scherf, U. *Materials Chemistry Frontiers* **2017**, *1*, 1118–1124.

(26) Oliveira, A. E. F.; Pereira, A. C.; Ferreira, L. F. *Talanta* **2023**, *252*, 123819.

(27) Ziyatdinova, G.; Guss, E.; Yakupova, E. *Sensors* **2021**, *21*, 8385.

(28) Zhou, Z.; Li, X.; Guo, D.; Shinde, D. B.; Lu, D.; Chen, L.; Liu, X.; Cao, L.; Aboalsaud, A. M.; Hu, Y., et al. *Nature Communications* **2020**, *11*, 5323.

(29) Zhou, Z.; Li, Z.; Rehman, L. M.; Lai, Z. *Chinese Journal of Chemical Engineering* **2022**.

(30) Aeiyach, S.; Lacaze, P. *Journal of Polymer Science Part A: Polymer Chemistry* **1989**, *27*, 515–526.

(31) Cysewska, K.; Karczewski, J.; Jasiński, P. *Electrochimica Acta* **2015**, *176*, 156–161.

(32) Giri, D.; Saha, S. K.; Siemons, N.; Anderson, I.; Yu, H.; Nelson, J.; Canjeevaram Balasubramanyam, R. K.; Patil, S. *ACS Applied Materials & Interfaces* **0000**, *0*, PMID: 37011231, null.

(33) Olean-Oliveira, A.; Brito, G. A. O.; Cardoso, C. X.; Teixeira, M. F. *Polymer* **2022**, *258*, 125291.

(34) Iroh, J. O.; Su, W. *Journal of applied polymer science* **1997**, *66*, 2433–2440.

(35) González-Tejera, M.; Carrillo, I.; Hernández-Fuentes, I. *Synthetic metals* **1998**, *92*, 187–195.

(36) Babaiee, M.; Pakshir, M.; Hashemi, B. *Synthetic Metals* **2015**, *199*, 110–120.

(37) Del Valle, M.; Ramıérez, A.; Hernández, L.; Armijo, F.; Dıéaz, F.; Arteaga, G. *Int. J. Electrochem. Sci* **2016**, *11*, 7048–7065.

(38) Mello, H. J. N. P. D.; Mulato, M. *Synthetic Metals* **2018**, *239*, 66–70.

(39) Charron, A.; Esnault, C.; Abada, Z.; Marcel, C.; Schmaltz, B.; Tran-Van, F. *Polymer International* **2018**, *67*, 684–690.

(40) Bai, S.; Hu, Q.; Zeng, Q.; Wang, M.; Wang, L. *ACS applied materials & interfaces* **2018**, *10*, 11319–11327.

(41) Khuyen, N. Q.; Zondaka, Z.; Harjo, M.; Torop, J.; Tamm, T.; Kiefer, R. *Polymers* **2019**, *11*, 849.

(42) Chen, J.; Yan, W.; Townsend, E. J.; Feng, J.; Pan, L.; Del Angel Hernandez, V.; Faul, C. F. *Angewandte Chemie International Edition* **2019**, *58*, 11715–11719.

(43) Mothika, V. S.; Räupke, A.; Brinkmann, K. O.; Riedl, T.; Brunklaus, G.; Scherf, U. *ACS Applied Nano Materials* **2018**, *1*, 6483–6492.

(44) Carbas, B. B.; Odabas, S.; Türksoy, F.; Tanyeli, C. *Electrochimica Acta* **2016**, *193*, 72–79.

(45) Zhang, X.; Zhen, S.; Zhang, L.; Chai, J.; Zou, L.; Xin, X.; Xu, J.; Zhang, G. *Polymer* **2020**, *202*, 122731.